# nature materials

Article

https://doi.org/10.1038/s41563-025-02268-w

# Plasmonic printing of high-performance metal oxide electronics under room temperature

Received: 23 October 2024

Accepted: 16 May 2025

Published online: 19 June 2025



Check for updates

Zhan Gao @ 1,7, Yang Fu @ 2,7, Qiang Zhang @ 1,3, Jian Li @ 1,4, Zhiyuan Li<sup>1</sup>, Guihuan Guo 📵 ¹, Dengfeng Li 📵 ¹, Jingkun Zhou 📵 ¹.⁴, Dangyuan Lei 🕲 ².⁵.⁶ 🖂 & Xinge Yu **©** 1,3,4,5 ⊠

Solution-processed metal oxide (MO) thin-film transistors present substantial promise for next-generation large-area, low-cost electronics. However, challenges like prolonged high-temperature annealing (at >400 °C) and a lack of universal, high-resolution printing technology hinder their widespread applications. Here we report a processing technology, termed 'plasmonic printing', for fabricating high-performance, solution-processed all-MO thin-film electronics under room temperature and ambient conditions. This process leverages femtosecond-laser-excited silver nanowires to induce plasmonic local heating, facilitating rapid (<0.3 s) and localized conversion of MO precursors into high-quality MO thin films, including conductor, dielectric and semiconductor. Remarkably, these MO thin films exhibit superior electrical performance without the requirement of special gases or high-temperature treatment, thereby enhancing the fabrication efficiency. Furthermore, precise pattern control is demonstrated, enabling the fabrication of high-density, solution-processed all-MO transistor arrays (48,400 transistors per square centimetre) and integrated logic gates with uniformity and precision. This technology presents a promising pathway for the cost-effective and high-throughput printing of high-density, complex, multilayered solution-processed MO electronics, delivering performance on par with vacuum-based counterparts.

Metal oxide (MO) thin films are a promising alternative to silicon for next-generation electronics<sup>1-3</sup>. Their high mobility, transparency, uniformity and flexibility enable applications in displays<sup>2</sup>, biosensors<sup>4</sup>, solar cells<sup>5</sup> and logic circuits<sup>6</sup>. Unlike silicon electronics using capital-intensive vacuum-based technologies, the solution processability of MO thin films offers great possibilities in high-throughput, low-cost and large-scale printing<sup>7</sup>. However, the challenge of printing high-quality MO lies in the requirement of prolonged high-temperature annealing at >400 °C, which is not suitable for efficient, continuous additive manufacturing<sup>7,8</sup>. This also hinders patterning MO into high-channel-count transistor arrays<sup>1</sup>.

To lower the processing temperature, various materials synthesis and processing methods such as combustion synthesis, alkoxide precursors and photoactivation process were developed<sup>8-17</sup>. Despite important technical progress, grand challenges remain. For example, thermal annealing at >200 °C is still needed with long periods of multiple processing steps, and no standardized method exists for producing high-quality, solution-processed MO thin films under room temperature

A full list of affiliations appears at the end of the paper. Me-mail: dangylei@cityu.edu.hk; xingeyu@cityu.edu.hk

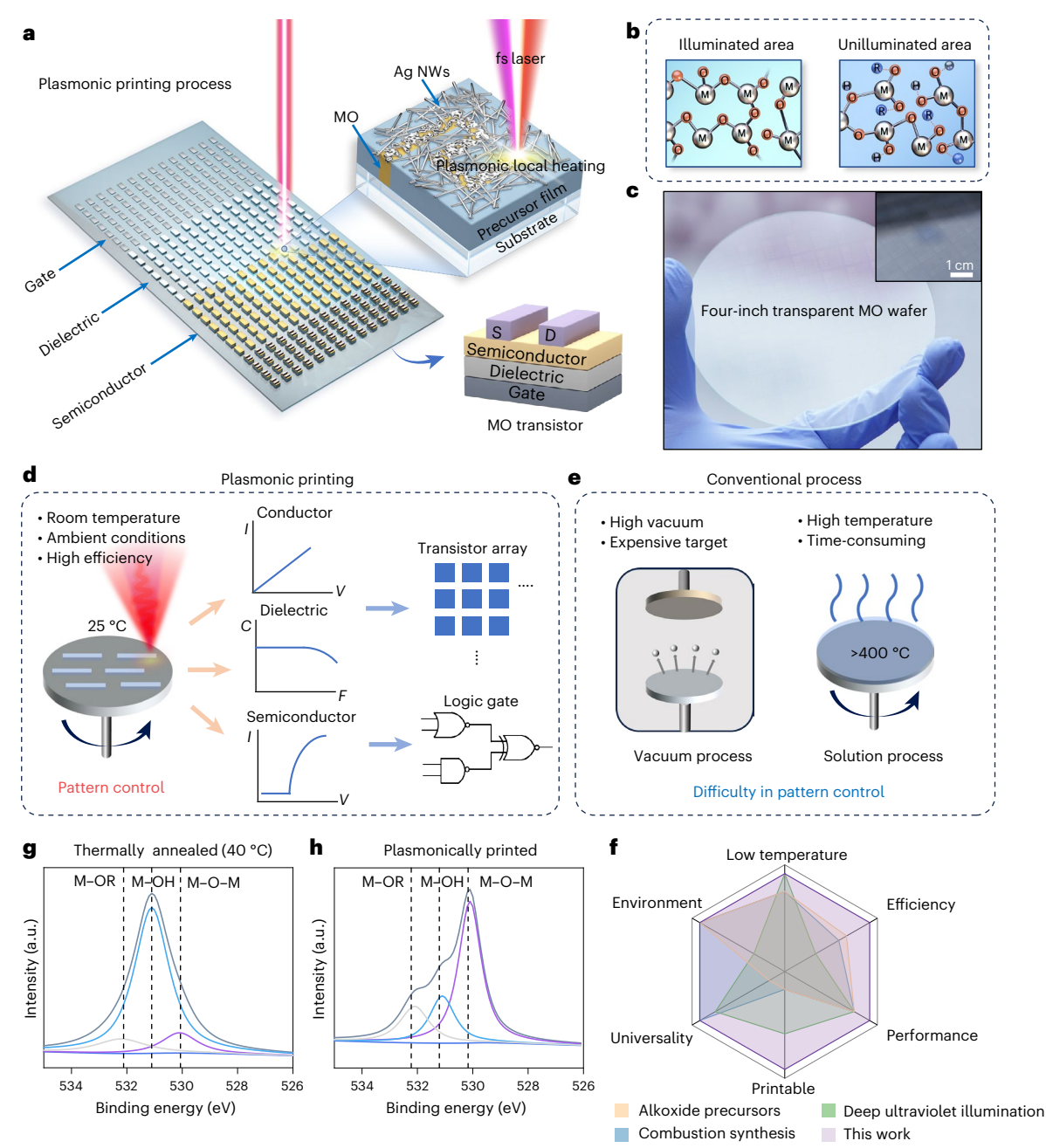


**Fig. 1**| **Plasmonic printing of solution-processed MO thin-film electronics. a**, Schematic illustration of the plasmonic printing process. Ultrafast, high-quality, localized MO conversion can be rapidly achieved under room temperature and ambient conditions, through the plasmon excitation of Ag NWs by a mixed fs laser beam to generate local heat for activating the formation of MO. After printing, excess Ag NWs can be physically wiped away, whereas the unconverted precursor can be etched away by 3% w/v OA. A printed transistor structure with a bottom gate and a top contact is illustrated in the bottom-right corner. **b**, Schematic of the chemical bonds within the illuminated area and unilluminated area of the MO thin film. M, metal cation; O, oxygen; H, hydrogen; R, alkyl group. **c**, Photograph of a four-inch wafer-scale transparent

MO array fabricated by the plasmonic printing process. Scale bar, 1 cm (inset).  $\mathbf{d}$ ,  $\mathbf{e}$ , Comparison of the plasmonic printing approach ( $\mathbf{d}$ ) and a conventional fabrication method ( $\mathbf{e}$ ) of MO thin films.  $\mathbf{f}$ , Radar comparison of the plasmonic printing process and three representative low-temperature solution processes for MO in terms of low-temperature processing, efficiency (time to achieve complete MO condensation), performance (conductivity, dielectric constant and mobility), printability (capability of pattern control of MO), universality (applicability across a wide range of MOs) and environment (processing atmosphere: the maximum value represents the ambient conditions).  $\mathbf{g}$ ,  $\mathbf{h}$ , O1s XPS results of 40 °C-annealed and plasmonically printed ITO (M-O-M lattice, 530.1 eV; M-OH metal hydroxide, 531.1 eV; M-OR bonds, 532.1 eV).

and ambient conditions<sup>3</sup>. Moreover, existing printing techniques cannot offer high-throughput, high-resolution processes for high-performance all-MO devices<sup>7,18,19</sup>. A recently developed promising method allows processing Ga-based liquid metal into large-area, flexible conductive  $GaO_x$  films under ambient conditions. While it can print various MO films, such as  $GaO_x$ , alumina  $(AlO_x)$  and indium oxide  $(InO_x)$ , this approach seems challenging, since Ga-based liquid metals lack key precursors<sup>20</sup>.

Here we report a new, universal printing technology, termed 'plasmonic printing' ('printing' emphasizes the additive and constructive nature of this technique, associated with forming patterns by inks), to address all the long-standing challenges in printed MO thin-film electronics. It uses plasmon-induced local heating to serve as the MO-forming energy and enables the rapid patterning of high-quality MO thin films, including conductors, insulators and semiconductors,

at room temperature and ambient conditions (Fig. 1a-c). A mixed (800 nm + 400 nm) femtosecond (fs) laser beam serves as the writing source to illuminate silver nanowires (Ag NWs) for generating remarkable plasmonic local heating. Combining plasmonic local heating and ultraviolet-induced photochemical reactions selectively convert illuminated MO precursors into condensed thin films. Using a motorized stage ensures the uniform, precise printing of high-quality, solution-processed MO films. Compared with conventional and other low-temperature solution processes of MO, the plasmonic printing process offers three crucial advantages (Fig. 1d-f). First, it operates entirely at room temperature and ambient conditions, requiring no special gases or high-temperature treatment. Second, the MO precursor locally converts into high-quality films within ~0.3 s (Fig. 1g,h), substantially improving the fabrication efficiency compared with slow vacuum deposition or prolonged high-temperature annealing. Meanwhile, the resulting MO thin films exhibit electrical performance comparable with those produced by vacuum-based processes. Third, it supports three high-precision patterning flows. Taking advantage of this universal process, a uniform, high-density all-MO thin-film transistor (TFT) array (48,400 transistors per square centimetre) and various basic logic gates are demonstrated.

### Overview of the plasmonic printing process

Extended Data Fig. 1a shows the plasmonic printing setup. A polarized 800-nm fs laser beam is focused by a lens and converted into a mixed 800-nm + 400-nm fs laser beam by a β-BaB<sub>2</sub>O<sub>4</sub> crystal. This mixed beam is then directed onto a sample positioned by a motorized three-axis stage. Before printing, MO precursor films are prepared by conventional sol-gel processes without high-temperature annealing (Methods). Subsequently, an ~700-nm-thick film of Ag NWs (Supplementary Fig. 1) is spray coated on the MO precursor film as the plasmonic local heat source. As shown in Extended Data Fig. 1b, three different process flows enable MO conversion. Process flow 1 requires no patterning of either the precursor film or Ag NW film. Instead, the laser spot size and movement control the printed MO size and shape. Process flow 2 patterns the precursor film via photolithography in advance, yielding regular MO films with smooth edges. Conversely, process flow 3 controls Ag NW patterns to define the MO film shape. This process lays the groundwork for nanoscale MO printing using plasmonic nanostructures as heat sources. In all the process flows, the unconverted precursor is removed by 3% w/v oxalic acid (OA). and Ag residues are wiped off (Supplementary Fig. 2). Time-of-flight secondary ion mass spectrometry (TOF-SIMS) was used to confirm no Ag residues in an indium tin oxide (ITO) sample. Two-dimensional TOF-SIMS ion mappings (Supplementary Fig. 3) show undetectable Ag<sup>+</sup> and strong In<sup>+</sup> and Sn<sup>+</sup> signals. The TOF-SIMS mass spectrum (Supplementary Fig. 4) further confirms that no Ag residues are detected in the plasmonically printed ITO film within the detection limit of TOF-SIMS. For multilayer devices, the process flows can be iterated on previously printed MO films.

#### Morphology-driven plasmonic local heating

To achieve the on-demand thermal treatment of MO thin films, a progressive plasmonic printing scheme is proposed by exploiting the morphology evolution of Ag NWs driven by their local heating and collective temperature rise under fs laser illumination. Leveraging the plasmonic heating effect requires a pre-spray-coated network of Ag NWs as heating intermedia. Plasmon-induced tight near-field confinement forms hot spots at the intersections of Ag NWs (Extended Data Fig. 2), triggering morphology evolution. Supplementary Fig. 5 shows the morphology changes in the plasmonic-heating-induced Ag nanostructures. At lower light intensities around the edge of the fs laser spot, long Ag NWs break into short ones. With near-field hot spots along these short Ag NWs (Extended Data Fig. 3), higher light intensities inside the laser spot melt them into small particles. The highest

intensities at the centre cause small, dense Ag particles to merge into larger, sparser ones. In particular, excessive heat can damage the MO thin films or even the glass substrate (Supplementary Fig. 6a). Therefore, an optimal light intensity is crucial<sup>21,22</sup>. The amount of Ag NWs also substantially influences its morphology evolution and the local heating effect (Supplementary Fig. 6b).

An infrared (IR) camera tracked the temporal temperature rise during plasmonic heating (Extended Data Fig. 1a and Supplementary Video 1). As shown in Fig. 2a and Supplementary Fig. 7, the local temperature of an illuminated region rises rapidly from 25 °C to ~360 °C in 66 ms and then drops to ~314 °C over 10 s due to the plasmonic heating-environment cooling balance. To understand such intriguing two-step heating process, scanning electron microscopy (SEM) was used to examine the Ag nanostructures before and after 0.1 s. 1 s and 10 s of laser irradiation (Fig. 2b-e). The Ag NW network melts into particles with varied sizes and densities during irradiation. Within 0.1 s, some Ag NWs form dense particles, whereas others melt into irregular assemblies. These then tend to merge into larger, sparser particles. Simulations based on the SEM images show that the pristine Ag NWs have the highest light absorption efficiency and, therefore, the largest rate of local temperature rise (Fig. 2f-i). However, since the plasmonic hot spots form at NW intersections, not at the NW-MO precursor interface (Fig. 2f), heat breaks the Ag NWs but does not treat the underlying MO precursors immediately. When the Ag NWs melt into small, dense particles within 0.1 s, the light absorption efficiency and local heating effect drop substantially but remain effective due to the collective contribution of the illuminated particles. This heating drives adjacent small particles/assemblies to merge into larger, sparser particles after 0.1 s (Fig. 2d,e), reducing the heat generation efficiency as morphology evolution completes (Fig. 2h,i). By contrast, isolated Ag particles exhibit a much lower temperature rise, regardless of their size and shape (Fig. 2j). However, dense Ag particle arrays with appropriate size and particle density can achieve in theory a temperature rise of over 2,000 K (Fig. 2k,l), providing instant yet sufficient thermal treatment for rapid MO precursor conversion.

# Characterizations of plasmonically printed MO thin films

Generally, thin-film electronics rely on conductors, dielectrics and semiconductors. Here plasmonic printing enables high-performance MO thin films and provides a universal strategy. Several representative MOs, including ITO, AlO<sub>x</sub>, indium-gallium-zinc oxide (IGZO), indium-zinc oxide (IZO) and InO<sub>x</sub> are prepared. X-ray photoelectron spectroscopy (XPS) was used to analyse metal-oxygen bonding in MOs before and after plasmonic printing (Fig. 1g,h, Extended Data Fig. 4 and Supplementary Figs. 8-12). The O1s peaks at 530.1 eV, 531.2 eV and 532.3 eV correspond to M-O-M lattices, M-OH species and M-OR species, respectively<sup>8,10,11</sup>. The 40 °C-dried ITO precursor film contains dominant densities of M-OH species, indicating incomplete oxidation. After the plasmonic printing process, the M-O-M peak at 530.1 eV intensifies, indicating successful conversion to dense ITO. Similar trends are observed for AlO<sub>x</sub>, IGZO, IZO and InO<sub>x</sub> (Extended Data Fig. 4), demonstrating the method's universality. No Ag peaks are observed in the XPS results of all the plasmonically printed MO films, further supporting the claim that Ag NWs can be completely removed at least to the detection limit of XPS. Grazing-incidence angle X-ray diffraction (GIAXRD) further evaluates the film crystallinity. Here ITO and  $InO_x$  thin films processed by low-temperature annealing (150 °C), high-temperature annealing (400 °C) and plasmonic printing are compared (Extended Data Fig. 5). Both 400 °C annealing and plasmonic printing yield the desired polycrystalline films, but the latter shows sharper Bragg peaks, indicating higher crystallinity. By contrast, AlO<sub>x</sub>, IGZO and IZO films remain amorphous after printing, as expected<sup>1</sup>. Overall, the XPS and GIAXRD results confirm that the quality of MO films printed within 0.3 s is comparable with that of MO films under 400 °C annealing for 1 h.

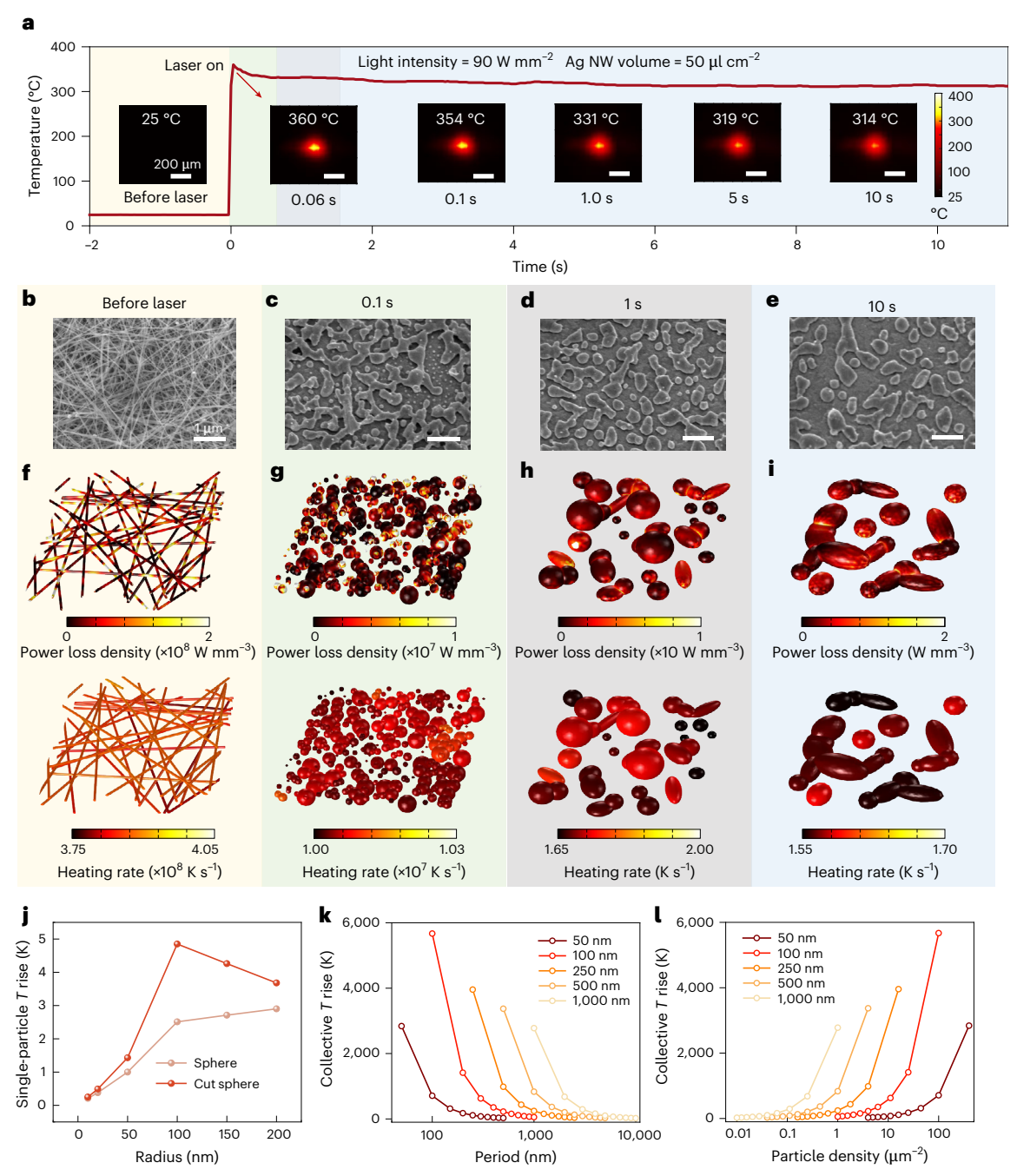


**Fig. 2** | **Progressive plasmonic heating mechanism. a**, Temporal temperature and IR photographs of Ag NWs under fs laser irradiation captured by a thermal imaging camera. **b**–**e**, SEM micrographs showing the morphology evolution of Ag NWs, from a pristine network structure before light illumination (**b**) to the hierarchical Ag particles after laser illumination for 0.1 s (**c**), 1 s (**d**) and 10 s

(e). f-i, Simulated light absorption intensity (top) and corresponding heat generation (bottom) for the structures in b-e (f-i, respectively). j, Calculated local temperature rise for a single Ag particle with varied sizes and shapes. k, l, Estimated collective local temperature rise for an array of Ag particles with varied sizes, periods (k) and particle densities (l).

#### Plasmonically printed MO thin-film electronics

XPS and GIAXRD measurements show great quality of the plasmonically printed MO thin films. We next investigated the electrical performance of these MO thin films across conductors, dielectrics and semiconductors. ITO, as the most common MO conductor, was first printed by optimizing the plasmonic printing parameters. We first examined the effect of ultraviolet-induced photochemical reactions (no Ag NWs)<sup>11,23,24</sup> on the ITO films (Supplementary Notes 1 and 2, Extended Data Fig. 6, Supplementary Figs. 13 and 14 and Supplementary Table 1). We found that mixed 800 + 400-nm fs pulses halved the resistance of 350 °C-annealed ITO, whereas 800 nm alone had no effect. This shows

the effectiveness of the 400-nm laser-induced photochemical reactions, which can enhance the quality and performance of MO thin films.

Next, plasmonic local heating was introduced by the laser excitation of the Ag NW film. We used process flow 1 to print individual MO functional layers, enabling direct pattern control and large-area fabrication via periodic laser scanning. Figure 3a shows visible traces on the Ag NW film due to their morphology changes. Removing residual Ag nanostructures revealed a 'CITYU' ITO pattern, demonstrating excellent patterning control. We then optimized the scan parameters for high-quality ITO films, using conductivity as the primary indicator of film quality. Narrow and long ITO channels (1.5 mm  $\times$  40  $\mu$ m  $\times$  12 nm)

were printed and their resistances were measured. Using rectangular prism modelling, we calculated the ITO conductivity (Supplementary Fig. 15). As noted, the photochemical reactions triggered by 400-nm light also enhance the quality of ITO after 350 °C annealing. With the same Ag NW-induced plasmonic local heating, we found that the conductivity of ITO printed with the 400 + 800-nm laser is approximately two times that of ITO printed with a pure 800-nm laser (Supplementary Fig. 16). This demonstrates that 400-nm-light-induced photochemical reactions can further enhance the electrical properties of ITO. Further optimization revealed that a 127 W mm $^{-2}$  fs laser with a primary wavelength of 800 nm was optimal for the plasmonic printing of MO (Supplementary Notes 3 and 4, Extended Data Figs. 6 and 7 and Supplementary Figs. 17–19).

We further optimized the scan parameters, namely, step length. dwell time and Ag NW thickness (Fig. 3b and Extended Data Fig. 6h,i). Conductivity drops sharply if the step size is <30 µm or the dwell time is >1 s. This results from morphological changes in the Ag NW during scanning (Fig. 2d,e and Supplementary Fig. 20). SEM images (Fig. 2d,e) show that Ag NWs transform into larger, irregular and continuous ellipsoidal structures after 1 s of irradiation, reducing the plasmonic heat generation capability. Supplementary Fig. 20 shows the morphologies of Ag NWs after dwell times of 5 s and 20 s. Prolonged irradiation causes the Ag NWs around the edges of the light spot to transform into irregular ellipsoidal shapes due to thermal conduction. When the light spot passes over these structures, the efficiency of plasmonic heat generation drops, lowering the ITO quality. To verify this, we profiled the surface of ITO printed under varied dwell times. Figure 3c and Supplementary Fig. 21 show that longer dwell times severely affect the surface morphology: dwell times of >1 s create a periodic topography with peaks and valleys; for dwell times from 1 s to 10 s, surface variation increases, indicating non-uniformity in the conversion of ITO. Weaker plasmonic heat generation results in lower conversion efficiency and thicker films, whereas stronger heat generation leads to more efficient conversion and thinner films<sup>25</sup>. Such an uneven conversion lowers the ITO conductivity. Likewise, shorter scanning steps reduce the plasmonic heat generation efficiency, also lowering the ITO conductivity. Consequently, we identified the optimal scanning parameters for ITO, achieving a maximum average conductivity of 1,763 S cm<sup>-1</sup> (comparable with commercial ITO glass (5,000 S cm<sup>-1</sup>)), and used the parameters for other MOs. Periodic bidirectional scanning suffices for preparing MO areas without parameter adjustment. For example, printing a 1-mm<sup>2</sup> ITO film takes ~1.6 min. Moreover, conductivity values measured at different probe distances (Extended Data Fig. 6j) are nearly identical, showing high uniformity.

Next, AlO<sub>x</sub> as the MO dielectric was processed by plasmonic printing. Figure 3d (inset) shows the dielectric testing of the AlO<sub>x</sub>:ITO/AlO<sub>x</sub>/ Cu sandwich with an electrode area of 0.1 × 1 mm<sup>2</sup>. Figure 3d-f shows the key dielectric properties: leakage current density (J-E), capacitance-voltage (C-V) and capacitance-frequency (C-F) curves of AlO<sub>x</sub> films. Laser path spacing was optimized for uniform coverage (Supplementary Note 4 and Supplementary Figs. 22 and 23). Dielectric properties can be improved by optimized strong light intensity with an ~9-V breakdown voltage, high capacitance (260 nF cm<sup>-2</sup> at 10 kHz) and stable frequency stability (10<sup>3</sup>–10<sup>6</sup> Hz). However, a further intensity increase showed no marked improvement in performance. Due to the low conversion temperature of AlO<sub>x</sub>, a light intensity of 8.6 W mm<sup>-2</sup> suffices. A higher intensity risks energy wastage and substrate damage. Therefore, the light intensity is set at 8.6 W mm<sup>-2</sup>. The measured thickness (Supplementary Fig. 24) and capacitance gave a dielectric constant of 8.8 for plasmonically printed AlO<sub>x</sub> films. This value is comparable with vacuum-prepared AlO<sub>x</sub> films, which surpasses 350 °C-annealed films (dielectric constant of 7.2; Supplementary Fig. 25).

Finally, based on the optimized printing parameter (Supplementary Note 4 and Supplementary Figs. 26 and 27), we printed MO semiconductors, including IGZO, IZO and InO, for transistors. The insets in

Fig. 3g–i show the transistor structures with ITO gate–glass substrate, associated with the  $AlO_x$  dielectric (annealed at  $350\,^{\circ}$ C,  $-120\,$ nm) and Al source–drain electrodes ( $40\,$ nm). Figure 3g–i shows the transfer and output curves of the TFTs based on plasmonically printed MO semiconductors. Supplementary Table 2 summarizes the comprehensive device parameters for these devices. All the printed semiconducting MO films exhibit good TFT performance, especially IGZO, with a saturation mobility ( $\mu_{sat}$ ) of  $21.0\pm3.2\,$ cm $^2$  V $^{-1}$  s $^{-1}$  and  $I_{on}/I_{off}\approx 10^4$ , surpassing  $350\,^{\circ}$ C-annealed devices (Supplementary Table 2 and Supplementary Fig. 28). In particular, in the plasmonically printed IZO- and InO $_x$ -based transistors, apparent negative-differential-resistance phenomena were observed under high gate voltage and bias. The underlying mechanisms are discussed in Supplementary Note 5.

Plasmonic printing offers a rapid and universal approach for the high-throughput fabrication of solution-processed MO conductors, dielectrics and semiconductors, with superior performance over thermal annealing due to localized plasmonic heating (Supplementary Note 6). It is worth mentioning that different MO precursor solutions necessitate different conversion temperatures, determining the laser intensity. Other processing parameters remain constant across MO materials (Supplementary Note 7). Meanwhile, the plasmonically printed high-quality MO films exhibit excellent environmental and thermal stability (Supplementary Note 8 and Supplementary Fig. 29).

Figure 3j-l and Supplementary Fig. 30 compare the performance of plasmonically printed MO devices with those from other low-temperature-solution- and vacuum-processed ones. Plasmonically printed MOs show obvious electrical performance advantages. To the best of our knowledge, plasmonically printed ITO achieves the highest conductivity (1,763 S cm<sup>-1</sup>) among the reported low-temperature-solution-processed works reported so far 10,13,26-34; the dielectric constant of plasmonically printed AlO<sub>x</sub> approaches ~9, which is also among the best<sup>8,29,35-48</sup>; and the  $\mu_{\text{sat}}$  value of transistors based on plasmonically printed IGZO, IZO and InO<sub>x</sub> are also among the highest values, comparable with vacuum-processed devices<sup>8,11,29,49-59</sup>. In particular, all-MO devices are printed under ambient conditions with much faster conversion (<0.3 s) than that of other methods. The process also enables precise, uniform and large-area fabrication (Supplementary Note 9 and Supplementary Figs. 31-33). These features are crucial for scalable, low-cost MO electronics.

# Plasmonically printed transistor arrays and logic circuits

IGZO, with a low power consumption and fast response, is a promising alternative to Si and, thus, commercially used in high-density TFT arrays for displays<sup>3</sup>. However, vacuum processing limits the scalability with high cost. We employ the plasmonic printing process to fabricate fully solution-processed high-density MO TFT arrays under room temperature and ambient conditions (Supplementary Fig. 34). Process flow 3 is first used to fabricate a  $10 \times 10$  ITO gate array  $(0.5 \times 0.5 \text{ mm}^2)$ each; Supplementary Fig. 35). Ag NWs are patterned to confine the plasmonic heating regions<sup>60</sup>. The uncondensed MO precursor film is easily removed through ~10 s of immersion in a 3% w/v OA solution. This immersion does not affect the electrical properties of the printed condensed ITO (Supplementary Fig. 36). Moreover, process flow 3 also enables smaller-scale arrays of ITO and AlO<sub>x</sub> (0.25 × 0.2 mm<sup>2</sup>). At reduced scales, the thermal conduction effects at the edges of the Ag NW patterns cause the non-uniformity of MO patterns (Supplementary Fig. 37). These irregularities could degrade performance in high-density arrays. Still, process flow 3 offers greater possibilities for printing nanoscale TFTs by patterning nanostructures on the MO precursor film. These nanostructures can induce local plasmonic heating to convert MOs at the nanoscale. Process flow 2 uses photolithography to pattern MO precursors with smooth edges. This flow ensures high resolution and edge quality (Supplementary Notes 10 and 11 and Supplementary Figs. 38 and 39). Additionally, our method yields better

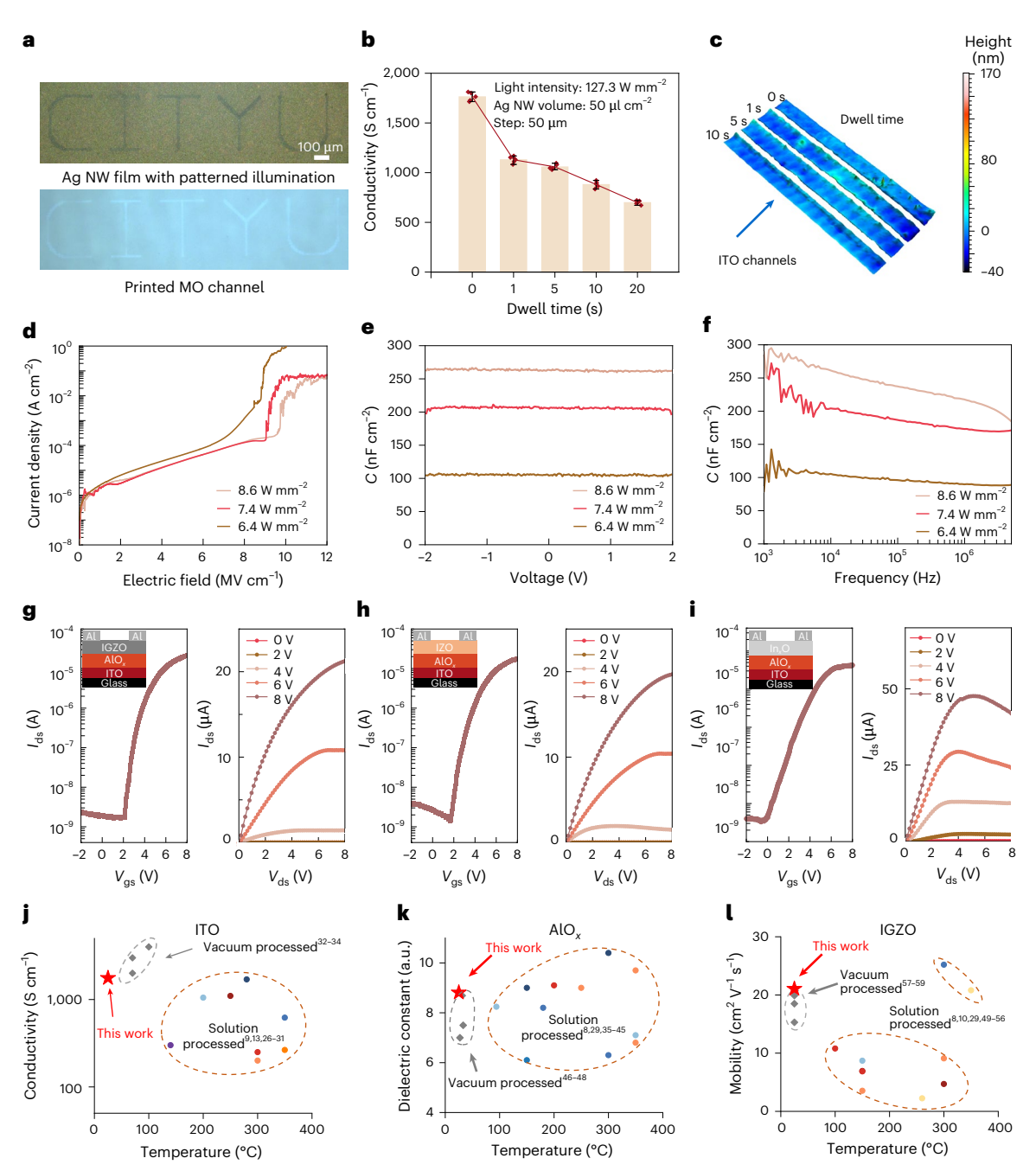


**Fig. 3** | **Plasmonically printed MO thin-film devices. a**, Top: photograph of a thin film of Ag NWs (on an ITO precursor film) after 'CITYU'-patterned laser illumination. Bottom: the same pattern is grafted onto the ITO precursor film through plasmonic printing to produce the printed ITO channel by laser scanning. **b**, Conductivity of the plasmonically printed ITO under different light-spot dwell times. Individual data points (n=5 per group) are overlaid to show the data distribution. Each point represents an independent ITO channel. Bar height, mean; error bars, standard deviation. **c**, Optical surface profiles of the plasmonically printed ITO channels under varied light-spot dwell times.  $\mathbf{d} - \mathbf{f}, J - E(\mathbf{d}), C - V(\mathbf{e})$  and  $C - F(\mathbf{f})$  characteristics of a plasmonically printed AlO $_x$ 

under different light illumination intensities.  $\mathbf{g}$ – $\mathbf{i}$ , Transfer characteristics ( $V_{ds}$  = 8 V) and output characteristics of transistors based on plasmonically printed IGZO ( $\mathbf{g}$ ), IZO ( $\mathbf{h}$ ) and InO $_x$ ( $\mathbf{i}$ ) channels, with their device configurations shown in the corresponding insets.  $\mathbf{j}$ – $\mathbf{l}$ , Comparison of the conductivity of ITO ( $\mathbf{j}$ ), dielectric constant of AlO $_x$ ( $\mathbf{k}$ ) and saturation mobility of IGZO ( $\mathbf{l}$ ) between our plasmonically printed samples and previously reported vacuum-based low-temperature-processed MO as a function of the processing temperature. Note that all the mobility values in  $\mathbf{l}$  are derived from IGZO transistors with AlO $_x$  as the dielectric layer.

uniformity and lower roughness than commercially used vacuum techniques (Supplementary Note 12 and Supplementary Fig. 40). As illustrated in Fig. 4a and Supplementary Figs. 41 and 42, an array of  $10 \times 10$  MO TFTs (ITO/AlO<sub>x</sub>/IGZO with width W = 150 µm and length L = 100 µm) is demonstrated with uniformly patterned features. To assess the reliability of the process, we evaluated the electrical performance of the  $10 \times 10$  plasmonically printed ITO gate electrodes,

AlO $_x$  dielectric layers and final IGZO-based TFTs (Fig. 4b–h and Supplementary Fig. 43). The results show that all these MOs exhibited great uniformity: ITO resistance, 11.8  $\pm$  6.3 k $\Omega$ ; AlO $_x$  dielectric constant, 8.03  $\pm$  0.8; IGZO  $\mu_{sat}$ , 14.5  $\pm$  5.4 cm $^2$  V $^1$  s $^{-1}$ . These results confirm -100% yield and uniform performance. This underscores the considerable potential of this technique for applications in the active-matrix technology.

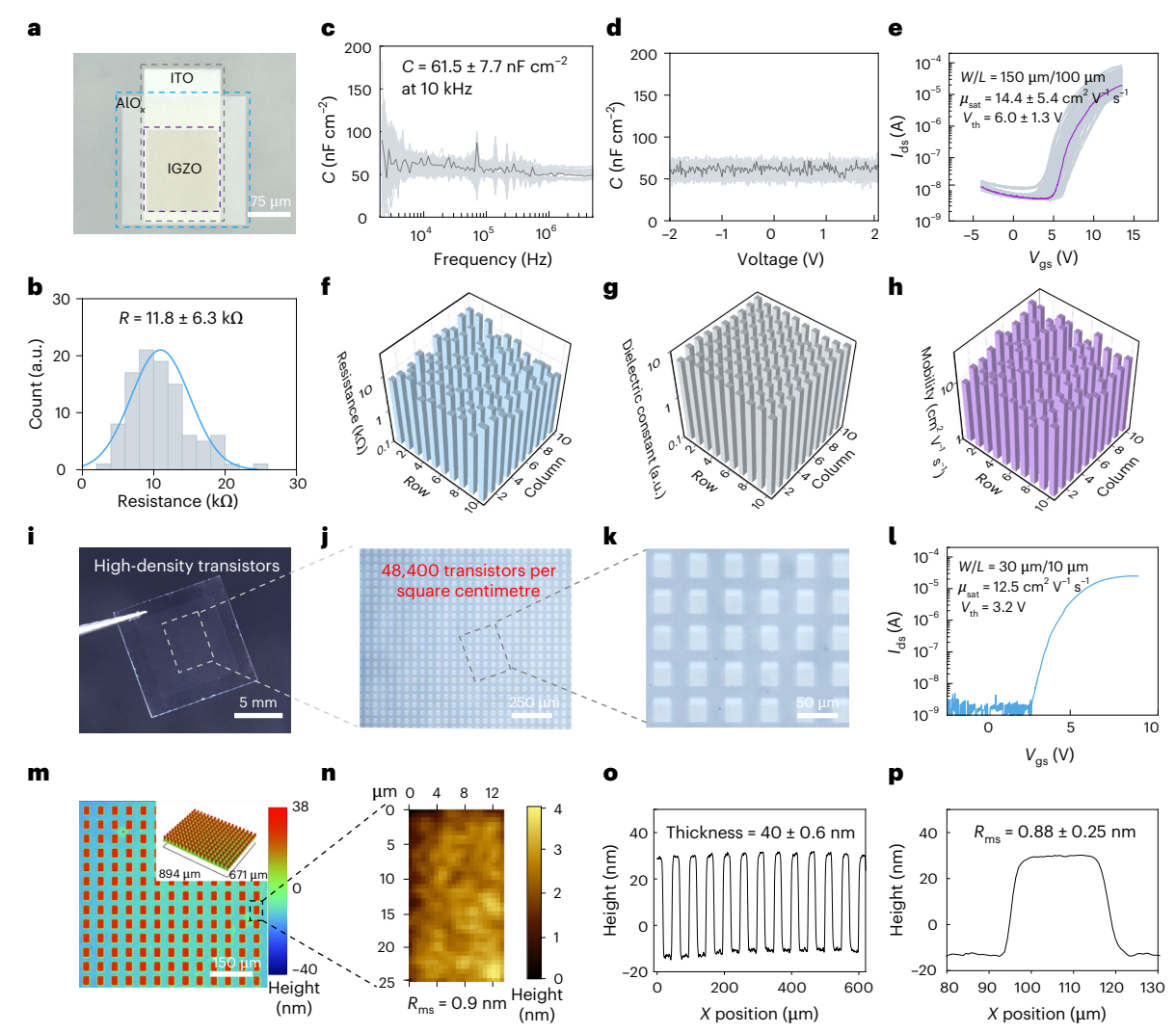


**Fig. 4** | **Plasmonically printed all-MO transistor arrays. a**, Microscope photograph of a plasmonically printed ITO gate/AlO $_x$  dielectric/IGZO semiconductor structure in a  $10 \times 10$  array. **b**, Resistance values of the plasmonically printed  $10 \times 10$  ITO gates, which were measured at the diagonal positions of each ITO square with a two-probe method. Resistance value is presented as mean  $\pm$  standard deviation. **c**,**d**, C–F(**c**) and C–V(**d**) characteristics of the plasmonically printed  $10 \times 10$  AlO $_x$  dielectrics, with the solid line representing a typical measurement curve. The capacitance value is presented as mean  $\pm$  standard deviation. **e**, Transfer characteristics of the plasmonically printed  $10 \times 10$  all-MO transistors, with the solid line representing a typical

measurement curve. Saturation mobility is presented as mean  $\pm$  standard deviation. **f**-**h**, Statistical distributions of resistance (**f**), dielectric constant (**g**) and mobility (**h**) of the  $10 \times 10$  plasmonically printed all-MO transistor array. **i**, Photograph of the plasmonically printed high-density all-MO transistor array and enlarged microscopy photograph in **j** and **k**. **l**, Representative transfer curve of a transistor in the high-density all-MO transistor array. **m,n**, Optical surface profile of the plasmonically printed high-density ITO gates. **o,p**, Height profile of the high-density ITO gates obtained from the optical surface profile in **m** (**o**), with an enlarged view shown in **p**. Thickness and  $R_{ms}$  values are presented as mean  $\pm$  standard deviation.

Next, we demonstrate the high-density, fully solution-processed MO transistor array (Fig. 4i–k) with a super-high resolution of 48,400 transistors per square centimetre at room temperature under ambient conditions. To the best of our knowledge, this density represents the highest level so far for a solution-processed MO transistor array. Each transistor has an ITO/AlO $_x$ /IGZO structure with a 30  $\mu$ m × 10  $\mu$ m channel. Figure 4l presents a representative transfer curve with  $\mu_{\rm sat}$  of 12.6 cm $^2$  V $^{-1}$  s $^{-1}$ ,  $V_{\rm th}$  of 3.2 V and  $I_{\rm on}/I_{\rm off}$  of  $^{-1}$ 0 $^4$ . An optical profilometer was used to examine the surface morphology and uniformity. As shown in Fig. 4m–p and Extended Data Fig. 8, the plasmonically printed units show uniform shape and thickness. The ITO surface is smooth, with root mean square ( $R_{\rm ms}$ ) roughness of 0.88  $\pm$  0.25 nm. These results confirm that Ag-NW-induced plasmonic heating enables uniform MO unit fabrication, crucial for high-density active-matrix applications.

Finally, plasmonic printing is used to fabricate all-MO-based logic circuits. Using process flow 2, we fabricate transistors as described

and pattern them into typical n-type metal-oxide-semiconductor logic gates. Figure 5a shows the schematic and optical photograph of the inverter based on plasmonically printed MO transistors (load transistor W/L = 1.5, drive transistor W/L = 15). Figure 5b,c presents the representative voltage transfer curves ( $V_{\text{out}}$ – $V_{\text{in}}$ ) and voltage gain curves under supply voltages  $V_{\rm DD}$  ranging from 6 V to 12 V, indicating good swing behaviour of inverter and gain of 15 at a  $V_{\rm DD}$  of 12 V. Supplementary Fig. 44 shows the inverter transient performance in the time domain. The input voltage is a square wave (1 kHz and 8 V) and  $V_{\rm DD}$  is 10 V. The inverters show good stability, fast switching, symmetric rise/fall edges and clear inversion. We also design and print logic NAND and NOR gates with the ideal logic function (Fig. 5d-g). The reliability of the plasmonic printing technique enables the design and printing of more complex circuits, such as a half-adder (Fig. 5h). Desired logic functions of the half-adder indicate that all the printed transistors function properly (Fig. 5i).

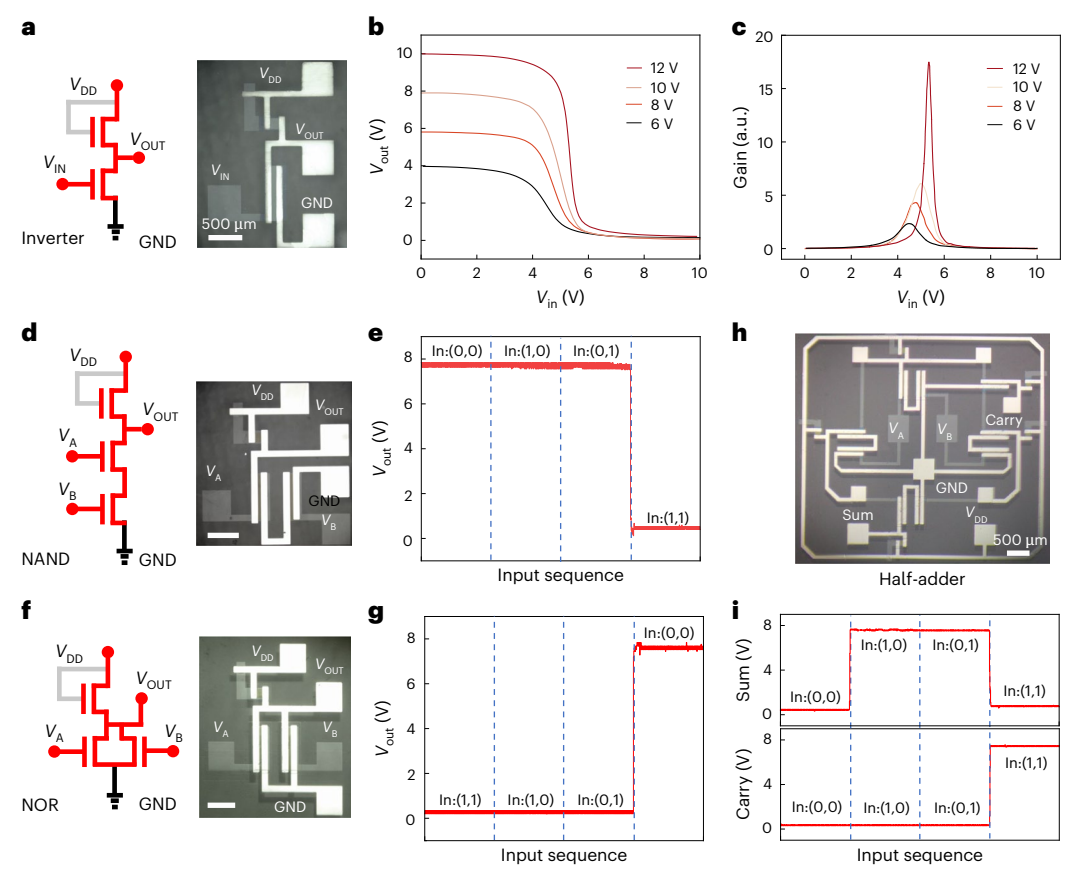


**Fig. 5** | **Plasmonically printed logic gates based on all-MO transistors. a**, Circuit diagram and microscope photograph of a plasmonically printed inverter. **b**, Curves of the output voltage versus input voltage of the inverter device at various  $V_{\rm DD}$  levels (6–12 V). **c**, Gain curves of the inverter device at various  $V_{\rm DD}$  levels (6–12 V). **d**, **e**, Circuit diagram and microscope image (**d**) of a plasmonically printed NAND gate and its output characteristics (**e**). Each input

sequence lasts for 60 s. Logic '0' and logic '1' are represented by 0 V and 10 V, respectively, which is the same for the subsequent logic devices.  $\mathbf{f.g.}$ , Circuit diagram and microscope photograph ( $\mathbf{f}$ ) of a plasmonically printed NOR gate and its output characteristics ( $\mathbf{g}$ ).  $\mathbf{h.i.}$ , Microscope image of a plasmonically printed half-adder ( $\mathbf{h}$ ) and its output characteristics ( $\mathbf{i}$ ).

#### Outlook

In this work, we have developed a new printing method for the high-throughput processing of high-performance MO thin films with super-high resolution, called plasmonic printing. It uses Ag-NW-induced plasmonic local heating, which affords comparable condensation/reaction energy of those based on thermal annealing at 300–400 °C, enabling great performance for electronics. Moreover, plasmonic printing universally applies to conductors, dielectrics and semiconductors at room temperature in ambient air. Its high yield and uniformity enable the fabrication of high-density MO TFT arrays and complex logic circuits. This breakthrough paves the way for commercializing low-cost solution-processed MO electronics, thereby fostering its extensive application in active-matrix pixilation, logic chip fields and many others.

### **Online content**

Any methods, additional references, Nature Portfolio reporting summaries, source data, extended data, supplementary information, acknowledgements, peer review information; details of author contributions and competing interests; and statements of data and code availability are available at https://doi.org/10.1038/s41563-025-02268-w.

#### References

 Yu, X., Marks, T. J. & Facchetti, A. Metal oxides for optoelectronic applications. Nat. Mater. 15, 383–396 (2016).

- . Kim, T. et al. Progress, challenges, and opportunities in oxide semiconductor devices: a key building block for applications ranging from display backplanes to 3D integrated semiconductor chips. Adv. Mater. 35, e2204663 (2023).
- Hosono, H. & Kumomi, H. Amorphous Oxide Semiconductors: IGZO and Related Materials for Display and Memory (John Wiley & Sons. 2022).
- Wang, B. et al. Flexible and stretchable metal oxide nanofiber networks for multimodal and monolithically integrated wearable electronics. *Nat. Commun.* 11, 2405 (2020).
- 5. Zheng, D. et al. Combustion synthesized zinc oxide electron-transport layers for efficient and stable perovskite solar cells. *Adv. Funct. Mater.* **29**, 1900265 (2019).
- 6. Biggs, J. et al. A natively flexible 32-bit Arm microprocessor. *Nature* **595**, 532–536 (2021).
- Park, J. W., Kang, B. H. & Kim, H. J. A review of low-temperature solution-processed metal oxide thin-film transistors for flexible electronics. *Adv. Funct. Mater.* 30, 1904632 (2019).
- Wang, B. et al. Expeditious, scalable solution growth of metal oxide films by combustion blade coating for flexible electronics. *Proc. Natl Acad. Sci. USA* 116, 9230–9238 (2019).
- Banger, K. K. et al. Low-temperature, high-performance solution-processed metal oxide thin-film transistors formed by a 'sol-gel on chip' process. Nat. Mater. 10, 45–50 (2011).

- Kim, M. G., Kanatzidis, M. G., Facchetti, A. & Marks, T. J. Low-temperature fabrication of high-performance metal oxide thin-film electronics via combustion processing. *Nat. Mater.* 10, 382–388 (2011).
- Kim, Y. H. et al. Flexible metal-oxide devices made by room-temperature photochemical activation of sol-gel films. Nature 489, 128–132 (2012).
- Yu, X. et al. Spray-combustion synthesis: efficient solution route to high-performance oxide transistors. *Proc. Natl Acad. Sci. USA* 112, 3217–3222 (2015).
- Datta, R. S. et al. Flexible two-dimensional indium tin oxide fabricated using a liquid metal printing technique. *Nat. Electron.* 3, 51–58 (2020).
- Teng, L.-F., Liu, P.-T., Lo, Y.-J. & Lee, Y.-J. Effects of microwave annealing on electrical enhancement of amorphous oxide semiconductor thin film transistor. *Appl. Phys. Lett.* 101, 132901 (2012).
- Ji, K. H. et al. Effect of high-pressure oxygen annealing on negative bias illumination stress-induced instability of InGaZnO thin film transistors. Appl. Phys. Lett. 98, 103509 (2011).
- Nakata, M. et al. Improvement of InGaZnO<sub>4</sub> thin film transistors characteristics utilizing excimer laser annealing. Appl. Phys. Express 2, 021102 (2009).
- Chen, H., Rim, Y. S., Jiang, C. & Yang, Y. Low-impurity high-performance solution-processed metal oxide semiconductors via a facile redox reaction. *Chem. Mater.* 27, 4713–4718 (2015).
- Scheideler, W. J., Kumar, R., Zeumault, A. R. & Subramanian, V. Low-temperature-processed printed metal oxide transistors based on pure aqueous inks. *Adv. Funct. Mater.* 27, 1606062 (2017).
- Park, J. & Moon, J. Control of colloidal particle deposit patterns within picoliter droplets ejected by ink-jet printing. *Langmuir* 22, 3506–3513 (2006).
- Kong, M. et al. Ambient printing of native oxides for ultrathin transparent flexible circuit boards. Science 385, 731–737 (2024).
- Lin, L. et al. In situ nanojoining of Y-and T-shaped silver nanowires structures using femtosecond laser radiation. *Nanotechnology* 27, 125201 (2016).
- Huang, H., Sivayoganathan, M., Duley, W. & Zhou, Y. High integrity interconnection of silver submicron/nanoparticles on silicon wafer by femtosecond laser irradiation. *Nanotechnology* 26, 025303 (2014).
- Rim, Y. S., Lim, H. S. & Kim, H. J. Low-temperature metal-oxide thin-film transistors formed by directly photopatternable and combustible solution synthesis. ACS Appl. Mater. Interfaces 5, 3565–3571 (2013).
- Huang, W. et al. Ultraviolet light-densified oxide-organic self-assembled dielectrics: processing thin-film transistors at room temperature. ACS Appl. Mater. Interfaces 13, 3445–3453 (2021).
- Park, S. et al. In-depth studies on rapid photochemical activation of various sol-gel metal oxide films for flexible transparent electronics. Adv. Funct. Mater. 25, 2807–2815 (2015).
- Tue, P. T., Inoue, S., Takamura, Y. & Shimoda, T. Combustion synthesized indium-tin-oxide (ITO) thin film for source/drain electrodes in all solution-processed oxide thin-film transistors. *Appl. Phys. A* 122, 623 (2016).
- Sunde, T. O. L. et al. Transparent and conducting ITO thin films by spin coating of an aqueous precursor solution. *J. Mater. Chem.* 22, 15740–15749 (2012).
- Lee, J. et al. A facile solution-phase approach to transparent and conducting ITO nanocrystal assemblies. J. Am. Chem. Soc. 134, 13410–13414 (2012).

- 29. Wang, B. et al. Solution-processed all-oxide transparent high-performance transistors fabricated by spray-combustion synthesis. *Adv. Electron. Mater.* **2**, 1500427 (2016).
- Song, L., Schenk, T., Defay, E. & Glinsek, S. Highly conductive low-temperature combustion-derived transparent indium tin oxide thin film. *Mater. Adv.* 2, 700–705 (2021).
- Ruan, C. et al. Lightwave irradiation-assisted low-temperature solution synthesis of indium-tin-oxide transparent conductive films. Ceram. Int. 48, 12317–12323 (2022).
- 32. Wong, F., Fung, M., Tong, S., Lee, C. & Lee, S. Flexible organic light-emitting device based on magnetron sputtered indium-tin-oxide on plastic substrate. *Thin Solid Films* **466**, 225–230 (2004).
- 33. Lin, Y.-C., Li, J. & Yen, W. Low temperature ITO thin film deposition on PES substrate using pulse magnetron sputtering. *Appl. Surf. Sci.* **254**, 3262–3268 (2008).
- 34. David, C., Tinkham, B., Prunici, P. & Panckow, A. Highly conductive and transparent ITO films deposited at low temperatures by pulsed d.c. magnetron sputtering from ceramic and metallic rotary targets. *Surf. Coat. Technol.* **314**, 113–117 (2017).
- Nayak, P. K., Hedhili, M. N., Cha, D. & Alshareef, H. N. High performance In<sub>2</sub>O<sub>3</sub> thin film transistors using chemically derived aluminum oxide dielectric. *Appl. Phys. Lett.* **103**, 033518 (2013).
- Branquinho, R. et al. Aqueous combustion synthesis of aluminum oxide thin films and application as gate dielectric in GZTO solution-based TFTs. ACS Appl. Mater. Interfaces 6, 19592–19599 (2014).
- 37. Jo, J.-W. et al. Highly stable and imperceptible electronics utilizing photoactivated heterogeneous sol-gel metal-oxide dielectrics and semiconductors. *Adv. Mater.* **27**, 1182–1188 (2015).
- Avis, C. & Jang, J. High-performance solution processed oxide TFT with aluminum oxide gate dielectric fabricated by a sol-gel method. J. Mater. Chem. 21, 10649–10652 (2011).
- 39. Xu, W., Wang, H., Ye, L. & Xu, J. The role of solution-processed high-κ gate dielectrics in electrical performance of oxide thin-film transistors. *J. Mater. Chem.* C **2**, 5389–5396 (2014).
- Xu, W. et al. Fully solution-processed metal oxide thin-film transistors via a low-temperature aqueous route. *Ceram. Int.* 43, 6130–6137 (2017).
- Carlos, E. et al. Printed, highly stable metal oxide thin-film transistors with ultra-thin high-κ oxide dielectric. Adv. Electron. Mater. 6, 1901071 (2020).
- Huh, J.-E. et al. Effects of process variables on aqueous-based AlO<sub>x</sub> insulators for high-performance solution-processed oxide thin-film transistors. J. Ind. Eng. Chem. 68, 117–123 (2018).
- 43. Carlos, E. et al. Laser induced ultrafast combustion synthesis of solution-based  ${\rm AlO}_{\rm x}$  for thin film transistors. J. Mater. Chem. C 8, 6176–6184 (2020).
- 44. Mu, Q. et al. A low-temperature solution-process high-*k* dielectric for high-performance flexible organic field-effect transistors. *Front. Mater.* **7**, 570002 (2020).
- Kumar, A. et al. Low-temperature solution-processed high-capacitance AlO<sub>x</sub> dielectrics for low-voltage carbon-based transistors. Org. Electron. 110, 106636 (2022).
- 46. Groner, M., Fabreguette, F., Elam, J. & George, S. Low-temperature  $Al_2O_3$  atomic layer deposition. *Chem. Mater.* **16**, 639–645 (2004).
- Voigt, M. & Sokolowski, M. Electrical properties of thin rf sputtered aluminum oxide films. *Mater. Sci. Eng. B* **109**, 99–103 (2004).
- 48. Liang, L. Y. et al. Substrate biasing effect on the physical properties of reactive RF-magnetron-sputtered aluminum oxide dielectric films on ITO glasses. ACS Appl. Mater. Interfaces 6, 2255–2261 (2014).

- Heo, J. S. et al. Water-mediated photochemical treatments for low-temperature passivation of metal-oxide thin-film transistors. ACS Appl. Mater. Interfaces 8, 10403–10412 (2016).
- Wang, H. et al. Low-temperature facile solution-processed gate dielectric for combustion derived oxide thin film transistors. RSC Adv. 4, 54729–54739 (2014).
- Bhalerao, S. R., Lupo, D. & Berger, P. R. Flexible thin film transistor (TFT) and circuits for Internet of Things (IoT) based on solution processed indium gallium zinc oxide (IGZO). In 2021 IEEE International Flexible Electronics Technology Conference (IFETC) 0023–0025 (IEEE, 2021).
- Kim, K. T. et al. An ultra-flexible solution-processed metal-oxide/ carbon nanotube complementary circuit amplifier with highly reliable electrical and mechanical stability. Adv. Electron. Mater. 6, 1900845 (2020).
- Xu, W. et al. Low temperature solution-processed IGZO thin-film transistors. Appl. Surf. Sci. 455, 554–560 (2018).
- 54. Jo, J.-W. et al. High-speed and low-temperature atmospheric photo-annealing of large-area solution-processed IGZO thin-film transistors by using programmable pulsed operation of xenon flash lamp. *J. Korean Phys. Soc.* **74**, 1052–1058 (2019).
- Jo, J.-W., Kim, K.-T., Facchetti, A., Kim, M.-G. & Park, S. K. High-quality solution-processed metal-oxide gate dielectrics realized with a photo-activated metal-oxide nanocluster precursor. *IEEE Electron Dev. Lett.* 39, 1668–1671 (2018).
- Carlos, E. et al. Boosting electrical performance of high-κ nanomultilayer dielectrics and electronic devices by combining solution combustion synthesis and UV irradiation. ACS Appl. Mater. interfaces 9, 40428–40437 (2017).

- Zheng, Z. et al. All-sputtered, flexible, bottom-gate IGZO/Al<sub>2</sub>O<sub>3</sub> bi-layer thin film transistors on PEN fabricated by a fully room temperature process. *J. Mater. Chem. C* 5, 7043–7050 (2017).
- 58. Ning, H. et al. Room-temperature fabrication of high-performance amorphous  $In-Ga-Zn-O/Al_2O_3$  thin-film transistors on ultrasmooth and clear nanopaper. ACS Appl. Mater. Interfaces **9**, 27792–27800 (2017).
- 59. Ning, H. et al. Facile room temperature routes to improve performance of IGZO thin-film transistors by an ultrathin  $Al_2O_3$  passivation layer. *IEEE Trans. Electron Dev.* **65**, 537–541 (2018).
- 60. Gao, Z. et al. Room-temperature-processed transparent hemispherical optoelectronic array for electronic eyes. *Mater. Today* **69**, 31–40 (2023).

**Publisher's note** Springer Nature remains neutral with regard to jurisdictional claims in published maps and institutional affiliations.

Springer Nature or its licensor (e.g. a society or other partner) holds exclusive rights to this article under a publishing agreement with the author(s) or other rightsholder(s); author self-archiving of the accepted manuscript version of this article is solely governed by the terms of such publishing agreement and applicable law.

@ The Author(s), under exclusive licence to Springer Nature Limited 2025

<sup>1</sup>Department of Biomedical Engineering, City University of Hong Kong, Hong Kong, China. <sup>2</sup>Department of Materials Science and Engineering, City University of Hong Kong, Hong Kong, China. <sup>3</sup>Institute of Digital Medicine, City University of Hong Kong, Kowloon, China. <sup>4</sup>Hong Kong Centre for Cerebro-Cardiovascular Health Engineering (COCHE), Hong Kong, China. <sup>5</sup>Hong Kong Institute for Clean Energy, City University of Hong Kong, Kowloon, China. <sup>6</sup>Department of Physics, Centre for Functional Photonics, and Hong Kong Branch of National Precious Metals Material Engineering Research Centre, City University of Hong Kong, Hong Kong, China. <sup>7</sup>These authors contributed equally: Zhan Gao, Yang Fu. ⊠e-mail: dangylei@cityu.edu.hk; xingeyu@cityu.edu.hk

#### Methods

#### **Precursor preparation**

All the MO precursor materials and 2-methoxyethanol were purchased from Sigma-Aldrich. Metal salts were dissolved in 2-methoxyethanol to generate the desired concentration. Also,  $60.2 \, \mathrm{mg \, ml^{-1}}$  of  $\ln(\mathrm{NO_3})_3 \cdot x H_2 \mathrm{O}$  solution was used for the  $\ln \mathrm{O_x}$  precursor. Furthermore, 150  $\mathrm{mg \, ml^{-1}}$  of  $\mathrm{Al}(\mathrm{NO_3})_3 \cdot x H_2 \mathrm{O}$  solution was used for the  $\mathrm{AlO_x}$  precursor. For the ITO precursor, 120.4  $\mathrm{mg \, ml^{-1}}$  of  $\ln(\mathrm{NO_3})_3 \cdot x H_2 \mathrm{O}$  solution and 75.6  $\mathrm{mg \, ml^{-1}}$  of  $\mathrm{SnCl_2}$  solution were mixed in a ratio of 9:1. For the IGZO precursor,  $60.2 \, \mathrm{mg \, ml^{-1}}$  of  $\ln(\mathrm{NO_3})_3 \cdot x H_2 \mathrm{O}$  solution around 37.8  $\mathrm{mg \, ml^{-1}}$  of  $\ln(\mathrm{NO_3})_3 \cdot x H_2 \mathrm{O}$  were mixed in a ratio of 3:1:1. For the IZO precursor,  $60.2 \, \mathrm{mg \, ml^{-1}}$  of  $\ln(\mathrm{NO_3})_3 \cdot x H_2 \mathrm{O}$  and 37.8  $\mathrm{mg \, ml^{-1}}$  of  $\ln(\mathrm{NO_3})_3 \cdot x H_2 \mathrm{O}$  were mixed in a ratio of 7:3. All the precursors were stirred at 25 °C overnight and filtered through 0.20- $\mu$ m syringe filters before film fabrication.

#### Optical setup for plasmonic printing process

As shown in Extended Data Fig. 1a, the optical setup includes a fs laser source (Chameleon Ultra II, Coherent) with a pulse duration of 140 fs and a repetition rate of 80 MHz, a pair of linear polarizers (LPVIS, Thorlabs) for intensity control, a convex lens (f=25 mm) to focus the laser spot and a  $\beta$ -BaB $_2$ O $_4$  crystal (thickness of 1 mm) in front of the focus for second-harmonic generation. The Ag NW-sprayed samples were mounted on a three-axis motorized stage for direct laser printing. The temperature data were recorded using an IR thermal camera (A325sc with Close-up 1x, FLIR). When extracting the temporal morphology, a mechanical shutter with a minimum open duration of -100 ms is placed right after the  $\beta$ -BaB $_2$ O $_4$  crystal for the required illumination time.

#### Plasmonic printing of MO thin films

Due to plasmonic heating generating extremely high localized temperatures in a very short time, the thermal stability of the substrate becomes the most critical factor when selecting a substrate. In Supplementary Note 13, Supplementary Figs. 45-47 and Supplementary Video 2, we compared various substrates for compatibility with the plasmonic printing process, and concluded that soda lime glass, with its excellent thermal stability and relatively poor thermal conductivity, is the best choice for this plasmonic printing process. Any subsequent references to glass specifically refer to soda lime glass. The glass substrates  $(1.5 \times 1.5 \text{ cm}^2, 0.7 \text{ mm thick})$  were first solvent cleaned and treated with energetic oxygen plasma for 5 min. For spin-coating fabrication, all the prepared precursors were spin coated at 2,000 rpm for 40 s in a chamber with the relative humidity controlled at 20% and dried at 40 °C for 6 h. Note that the drying process here is aimed at removing solvents of the wet precursor film, allowing it to air dry and become more solid for subsequent processing. To achieve a completely dried precursor film, lower dry temperatures require longer durations (40 °C for 6 h), whereas higher dry temperatures require shorter durations (150 °C for 5 min). However, the final device performance remains similar (Supplementary Fig. 48). If necessary, these processes were repeated to achieve the desired film thickness. Process flow 1 (Extended Data Fig. 1b) was used for the printing of single, functional MO layers. The Ag NW solution (5 mg ml<sup>-1</sup> in ethanol) was purchased from XFNANO and used as received. Different thicknesses of Ag NW films, which were measured as per the volume of the Ag NW solution sprayed per unit area (20-70 µl cm<sup>-2</sup>), were sprayed onto the precursor film with a discharge speed of 40 ml per 30 s by an IWATA HP-CP spray gun (0.3 mm) at an air pressure of 15 psi. Next, the sample was secured onto a high-precision three-dimensional electrically controlled stage, allowing control over the parameters of the laser spot scanning, including spot size, step size and spot dwell time. After laser scanning, the residual Ag nanostructures were wiped away with a dust-free cloth. For the printing and performance measurements of ITO, the laser spot was scanned along a long and narrow path on the Ag NW film, thereby printing an ITO conductive channel (1.5 mm

long, 40 µm wide). Subsequently, with the assistance of a metal mask, 60-nm-thick Cu electrodes were sputtered at both ends of the ITO channel, and the resistance of ITO was measured using a probe station and DAQ6510. As described in the main text, the optimized scanning parameters for ITO were as follows: step size of 50 um, dwell time of 0 s, Ag NW volume of 50  $\mu$ l cm<sup>-2</sup> and light intensity of 127.3 W mm<sup>-2</sup>. These parameters were applied to the preparation of other MOs, with only the light power density being adjusted based on the temperature required for the conversion of different precursors. For the printing and performance measurements of AlO<sub>x</sub>, commercial ITO glass was used instead of pure glass as the substrate, and the AlO<sub>x</sub> precursor film and the Ag NW film were prepared as previously described. Subsequently, laser scanning was performed periodically back and forth on the Ag NW film to scan out a square area of approximately 0.5 mm<sup>2</sup>. Following this, Cu electrodes (0.1 × 1 mm<sup>2</sup>) were deposited within the region using a metal mask. Then, the J-E, C-V and C-F curves were measured using a Keysight B1500A semiconductor analyser. For the printing and performance measurements of InO<sub>x</sub>, IZO and IGZO, commercial ITO glass was used as the substrate followed by the fabrication of an ~120-nm 350 °C-annealed AlO<sub>x</sub> film as the dielectric layer. Then, InO<sub>x</sub>, IZO and IGZO precursor films and the Ag NW film were prepared as previously described. Laser scanning was performed periodically back and forth on the Ag NW film to scan out a square area of approximately 1 mm<sup>2</sup>. Following this, Al electrodes ( $W = 150 \, \mu \text{m}$ ,  $L = 100 \, \mu \text{m}$ ) were deposited within the region using a metal mask by an electron beam. Then, the transfer and output characteristic curves were measured using the Keysight B1500A semiconductor analyser. The  $\mu_{\text{sat}}$  values in the saturation regime are calculated using the standard equation:

$$I_{\rm D} = \frac{W}{2L} \mu_{\rm sat} C (V_{\rm G} - V_{\rm T})^2,$$

where  $I_D$  is the source–drain current; C is the capacitance per unit area of the dielectric layer;  $V_T$  is the threshold voltage;  $V_G$  is the gate voltage; and W and L are the channel width and length, respectively. The average quasi-static capacitance of the high-temperature-annealed  $AlO_x$  films (49 nF cm<sup>-2</sup> over 0.1–10 Hz; Supplementary Fig. 49 and Supplementary Note 14) was measured by Novocontrol Concept 80 under 0.5 V, which was used to calculate the saturation mobility for all the transistors based on individually plasmonically printed semiconductors. To better evaluate the intrinsic mobility of the semiconductor channel, we also calculated and thoroughly discussed the linear mobility of the transistor (Supplementary Fig. 50 and Supplementary Note 14).

#### Plasmonic printing of MO TFT array and logic gates

The fabrication of the precursor film was the same as described above. As shown in Extended Data Fig. 1b, process flows 2 and 3 were used to fabricate the MO arrays. In process flow 2, photolithography was applied to pattern the precursor film. AZ 4620 (AZ Electronic Materials) was spin coated at 3,000 rpm for 40 s on the precursor film, annealed at 100 °C for 5 min and exposed to ultraviolet light through a designed photomask. After development in the AZ 400K developer (volume ratio of 1:4 with water), the substrate was immersed in 3% w/v OA for 10 s to remove the exposed precursor film. Subsequent removal of the residual photoresist was carried out using acetone, resulting in the desired precursor array geometry. Next, a certain thickness of Ag NW film  $(50 \,\mu l\,cm^{-2})$  was sprayed onto the substrate. The laser spot was then programmed to scan only the areas with precursor arrays, followed by wiping off the residual Ag nanostructures. This process was repeated to fabricate multilayered MO functional layers. Finally, Ag electrodes were fabricated by electron beam and patterned by photolithography. The transfer curves of the  $10 \times 10$  MO transistor array and high-density MO transistor were measured by the Keysight B1500A semiconductor analyser. The average quasi-static capacitance of the plasmonically AlO<sub>x</sub> films (64 nF cm<sup>-2</sup> over 0.1–10 Hz; Supplementary Note 14) was used for

saturation mobility calculation of the transistor array. The resistance values of 100 ITO gates were measured at their diagonal positions using a two-probe method. The C-V and C-F characteristics of 100 AlO<sub>x</sub> films were measured by the Keysight B1500A semiconductor analyser after plasmonically printing AlO<sub>x</sub> arrays on ITO glass and then depositing the metal electrodes. Process flow 2 was also applied to fabricate the logic gates as described above. The logic function of the devices was tested by an oscilloscope. In process flow 3, after preparation of the precursor film, 50 µl cm<sup>-2</sup> of the Ag NW film was sprayed onto the precursor film with the designed metal mask to form a patterned Ag NW film array (Supplementary Fig. 37). Subsequently, the laser spot was programmed to scan only the areas with Ag NWs. After wiping the residual Ag nanostructures, the substrate was immersed in 3% w/v OA for 10 s to remove the unconverted precursor film, leaving behind the converted MO. In the experiment of comparing the structural properties between plasmonically printed MO and commercial customized MO by using vacuum-based methods, the commercial ITO film was fabricated using a robust vacuum sputtering process, and the patterning of ITO was achieved via laser etching technology.

#### Film characterization

The TOF-SIMS results were measured using ION TOF-SIMS 5. The XPS results were measured using Thermo Fisher ESCALAB 250Xi. The vacuum level in the analysis chamber is maintained at  $8\times10^{-10}$  Pa, and the excitation source utilizes Al K $\alpha$  radiation (hv = 1,486.6 eV). GIAXRD measurements were conducted by a Rigaku SmartLab device (9KW). All the MO samples used for the XPS and GIAXRD measurements were printed using optimal printing parameters. The surface morphologies were measured using top-view SEM (FEI Quanta 450 FESEM) and optical surface profiler.

#### **Electric-field simulation**

The electric-field distribution in two intersecting Ag NWs is simulated using finite-difference time-domain to build infinitely long nanowires. The incident light is a plane wave. To mimic the randomly oriented Ag NWs within the network, the incident polarization is set at  $45^\circ$  with respect to the axis of one NW, and the angle of intersection between the two NWs varies from  $0^\circ$  to  $90^\circ$ . No substrate is built in the simulation model since the Ag NWs are mostly floating unless intersecting with other wires. For the short Ag NWs with side dumbbells, the size of the side dumbbells increases when reducing the length of the middle part, to maintain the total amount of Ag. In this case, a glass substrate is built in the model since these structures would not float. An air gap of 2 nm is set between the glass substrate and the structures to avoid singularities in the simulation.

#### Light absorption and heat generation simulation

To depict the morphology-driven heating processes, we performed multiphysics simulations (COMSOL) for four states of the Ag nanostructures (before and after light illumination for 0.1 s, 1 s and 10 s). The simulated structures are built within a 2  $\mu$ m  $\times$  2  $\mu$ m area based on the SEM images. Two 'electromagnetic waves, frequency domain' modules are applied to obtain the volumetric light absorption intensity of the structures. The first step only consists of air and glass for calculating the reflection of an incident transverse-electric wave by the substrate, which is then utilized, in the second step, as a background field for simulating the scattering field and power loss density of the Ag nanostructures on the substrate. The incident light intensity is set as 636 W m $^{-2}$ . The refractive index of Ag is obtained from ref. 61, and the refractive index of glass is set as 1.45. Afterwards, the 'heat transfer

in solids and fluids' module is applied to obtain the temperature distribution by inputting the volumetric heat source obtained above. The environmental air speed and ambient temperature are set as  $0.1\,\mathrm{m\ s^{-1}}$  and  $293.15\,\mathrm{K}$ , respectively.

### **Data availability**

All data needed to evaluate the conclusions in this study are present in the Article and its Supplementary Information. Source data are provided with this paper.

#### References

61. Johnson, P. B. et al. Optical constants of the noble metals. *Phys. Rev. B* **6**, 4370 (1972).

#### **Acknowledgements**

This work was supported by the Foundation of National Natural Science Foundation of China (NSFC) (grant nos. 61421002 and 62022001), the Research Grants Council of the Hong Kong Special Administrative Region (grant nos. 11213721, AoE/P-502/20, 11215722, 1121523, A-CityU101/20 and RFS2324-1S03), City University of Hong Kong (grant nos. 9229055, 9610444, 9678274, 9680322, 9667246 and 9360165), the Nano & Material Technology Development Program through the National Research Foundation of Korea (NRF) funded by the Ministry of Science and ICT (no. RS-2024-00411904), in part by the InnoHK Project on Project 2.2—Al-based three-dimensional ultrasound imaging algorithm at the Hong Kong Centre for Cerebro-Cardiovascular Health Engineering (COCHE), and the Innovation and Technology Commission of Hong Kong (grant no. MHP/162/22).

#### **Author contributions**

Z.G. and Y.F. contributed equally to this work. X.Y., D. Lei., Z.G. and Y.F. conceived the ideas. X.Y., Z.G., Y.F. and D. Lei. designed the experiments. Z.G. and Y.F. carried out the device fabrication. Z.G. carried out the device measurements, film characterizations and device demonstrations. Z.G. and Y.F. analysed the experimental data. Y.F. performed the physical simulation and thermal analysis. Z.G., Y.F., D. Lei. and X.Y. wrote the paper. All other authors contributed to discussing the data and commenting on the paper.

#### **Competing interests**

The authors declare no competing interests.

#### **Additional information**

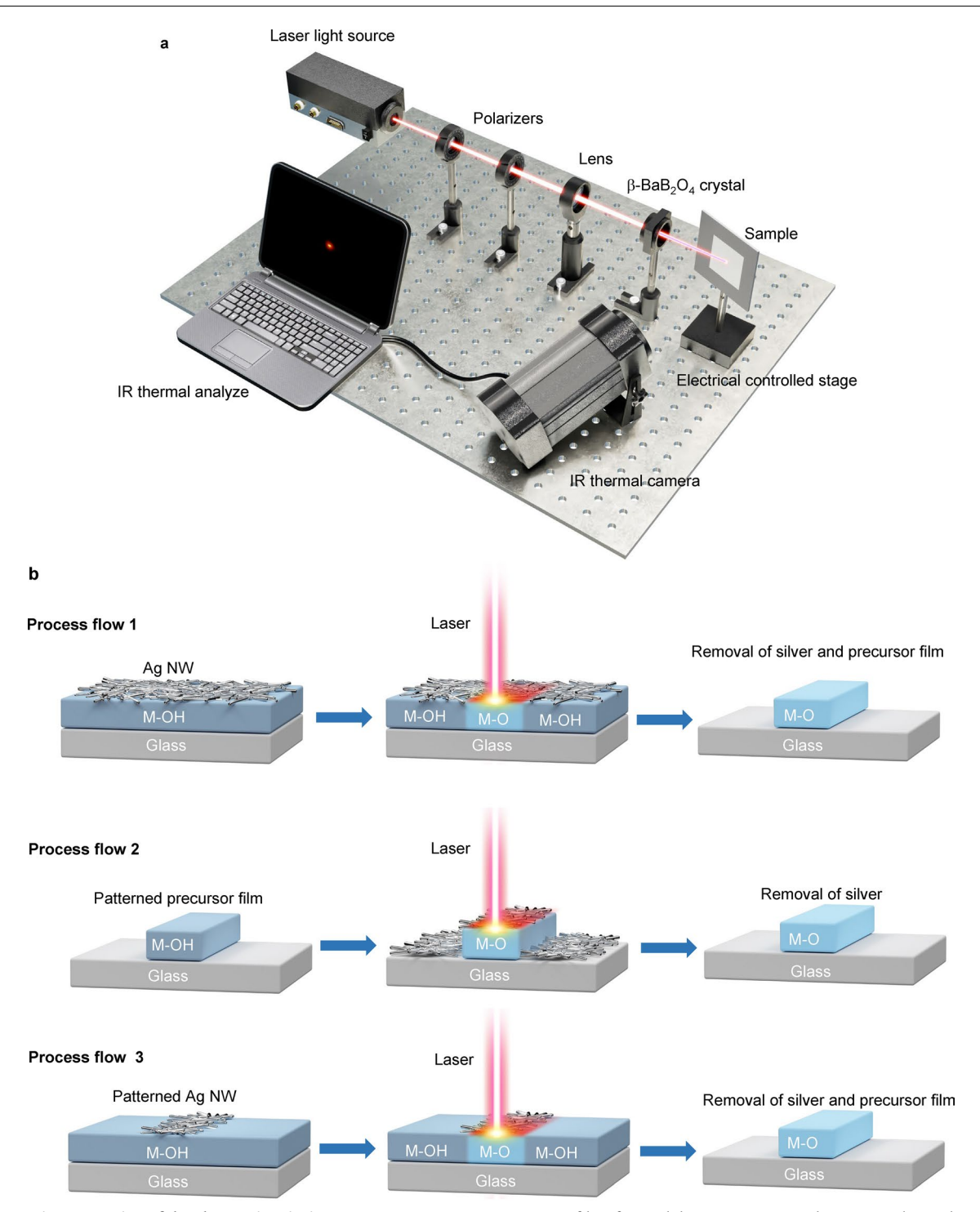
**Extended data** is available for this paper at https://doi.org/10.1038/s41563-025-02268-w.

**Supplementary information** The online version contains supplementary material available at https://doi.org/10.1038/s41563-025-02268-w.

**Correspondence and requests for materials** should be addressed to Dangyuan Lei or Xinge Yu.

**Peer review information** *Nature Materials* thanks Michael Dickey, Vivek Subramanian and the other, anonymous, reviewer(s) for their contribution to the peer review of this work.

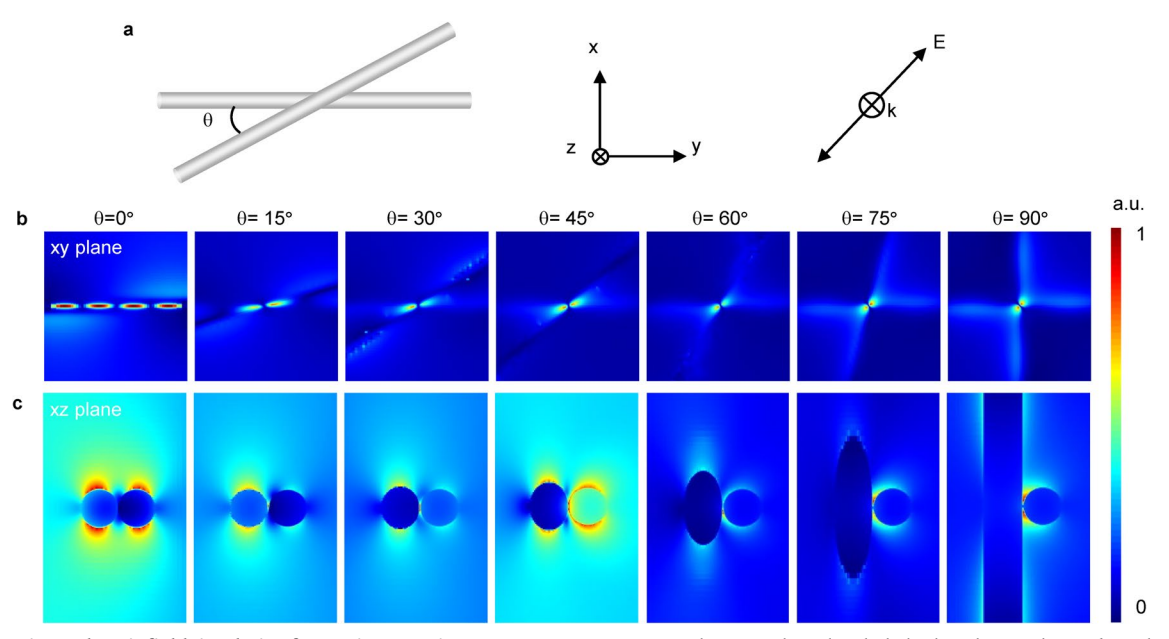
**Reprints and permissions information** is available at www.nature.com/reprints.



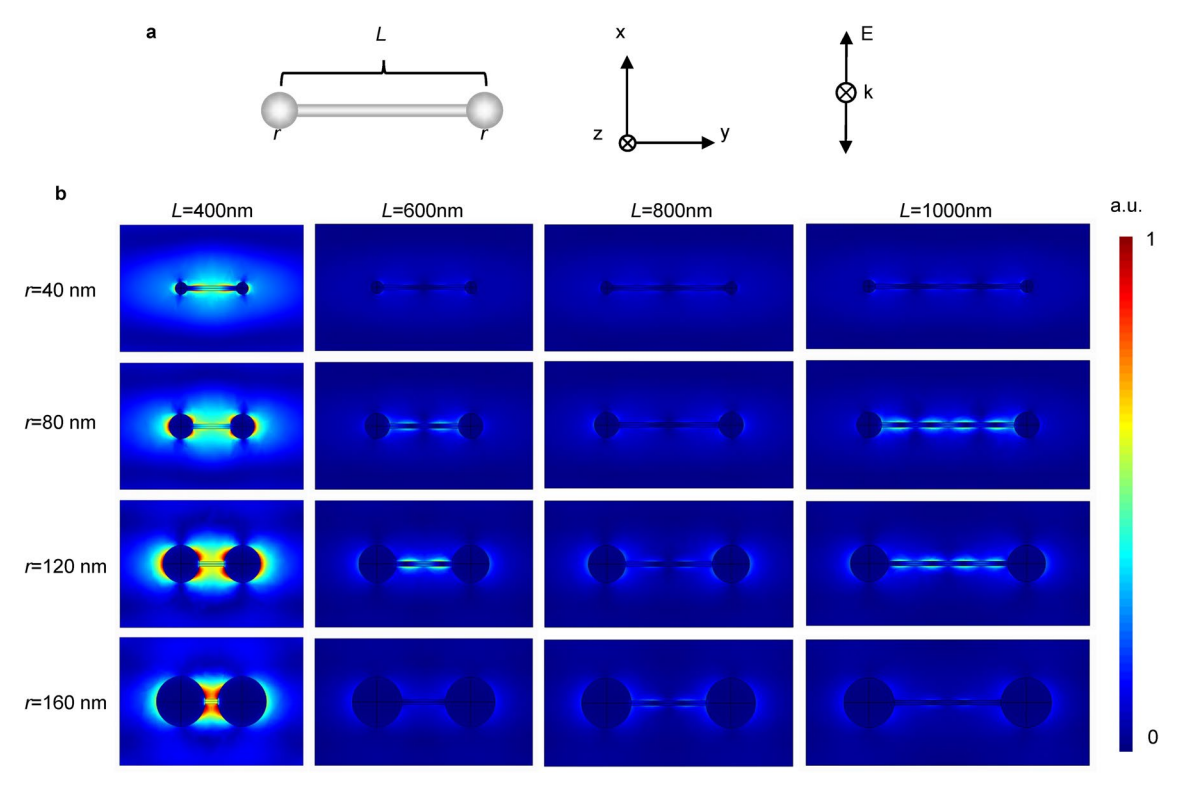
## Extended Data Fig. 1 | Overview of the plasmonic printing process.

- **a**, Schematic illustration of the optical setup for the plasmonic printing.
- $\textbf{b}, Three \ plasmonic \ printing \ process \ flows. \ 'M-OH' \ represents \ the \ unconverted$

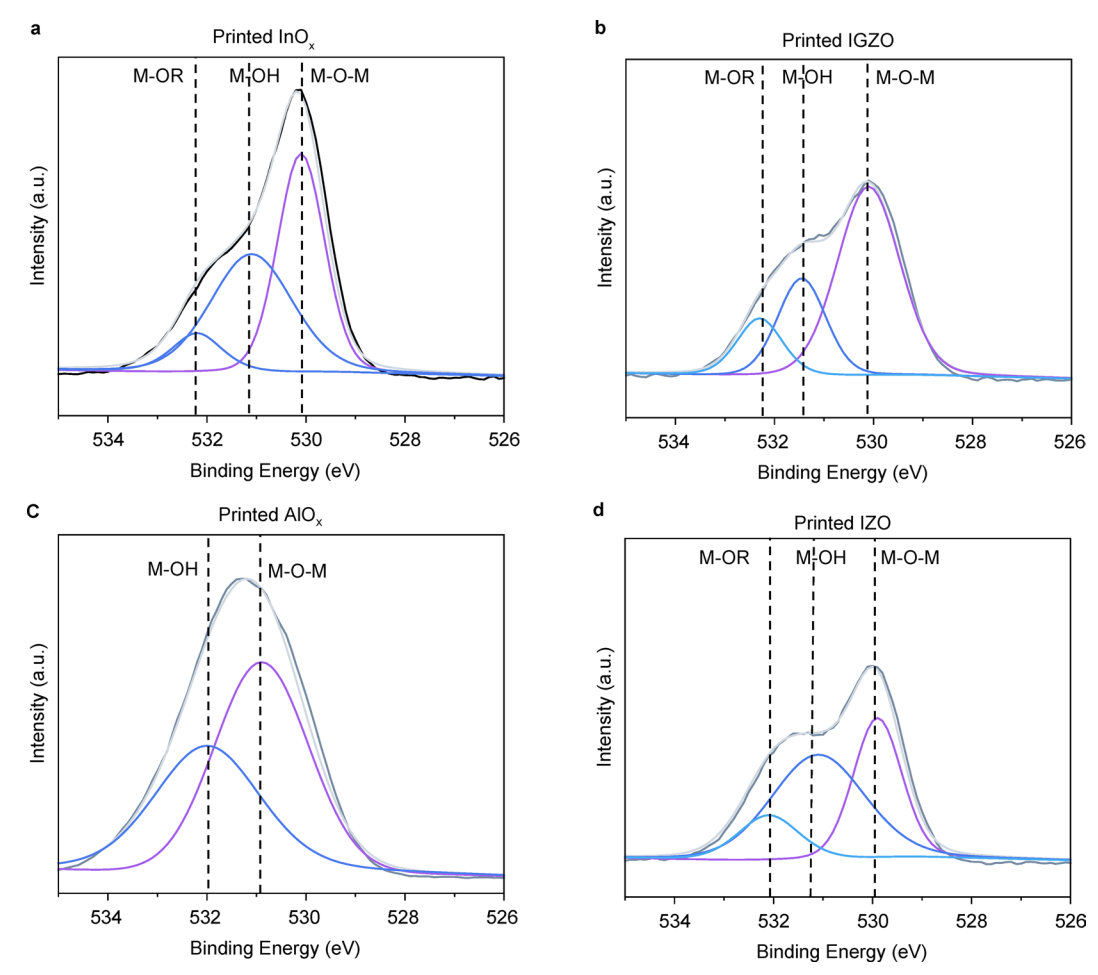
precursor film of MO, while 'M-O' represents the converted MO. The remaining Ag nanostructures in each flow are physically wiped off, and the remaining precursor film is removed by soaking in 3% w/v OA.



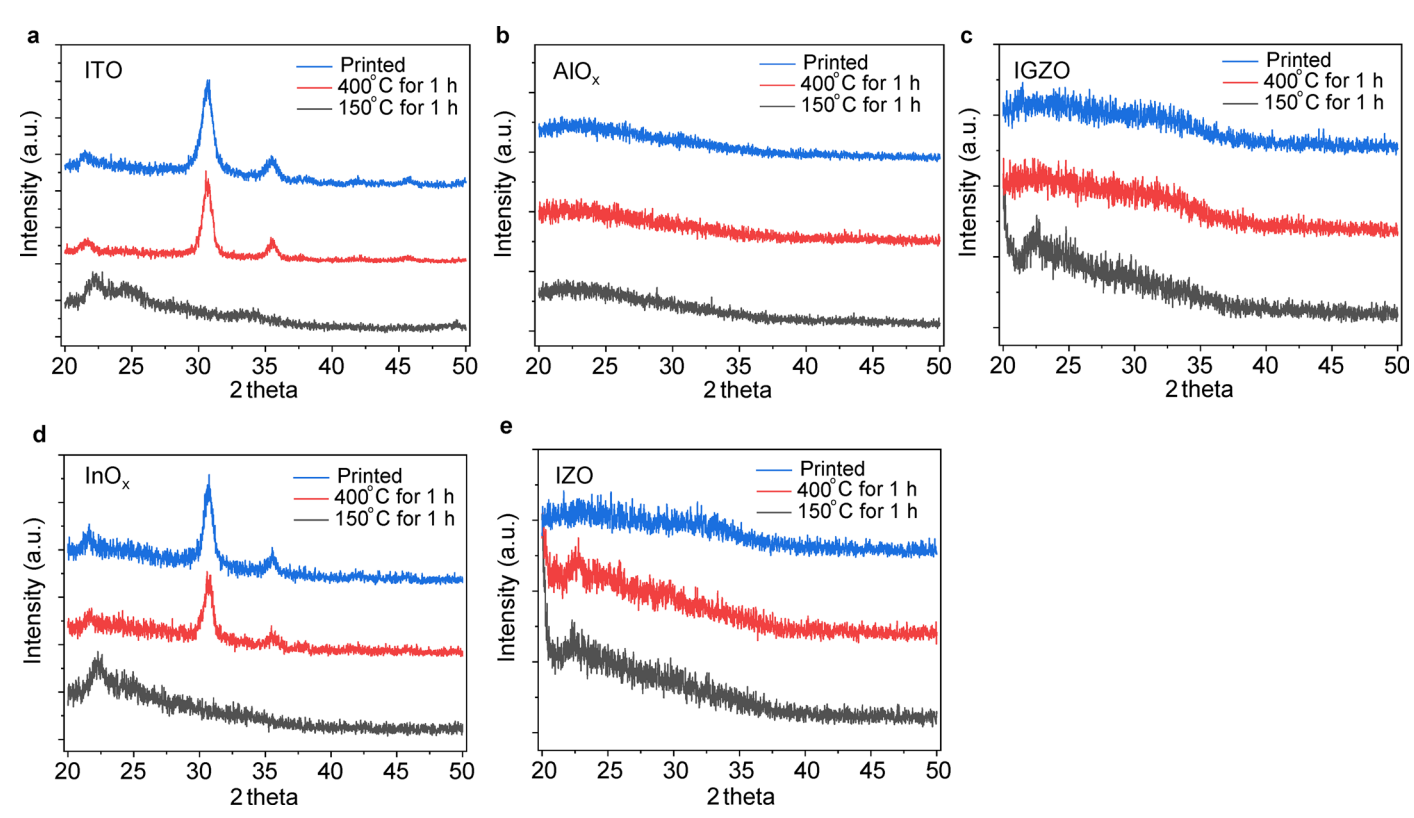
Extended Data Fig. 2 | Electric field simulation for two intersecting Ag NWs. a, Structure, coordinate, and incident light built in the simulation. b, c, Electric field distribution profiles in the x-z and x-y planes for structures with varied angle of intersection.



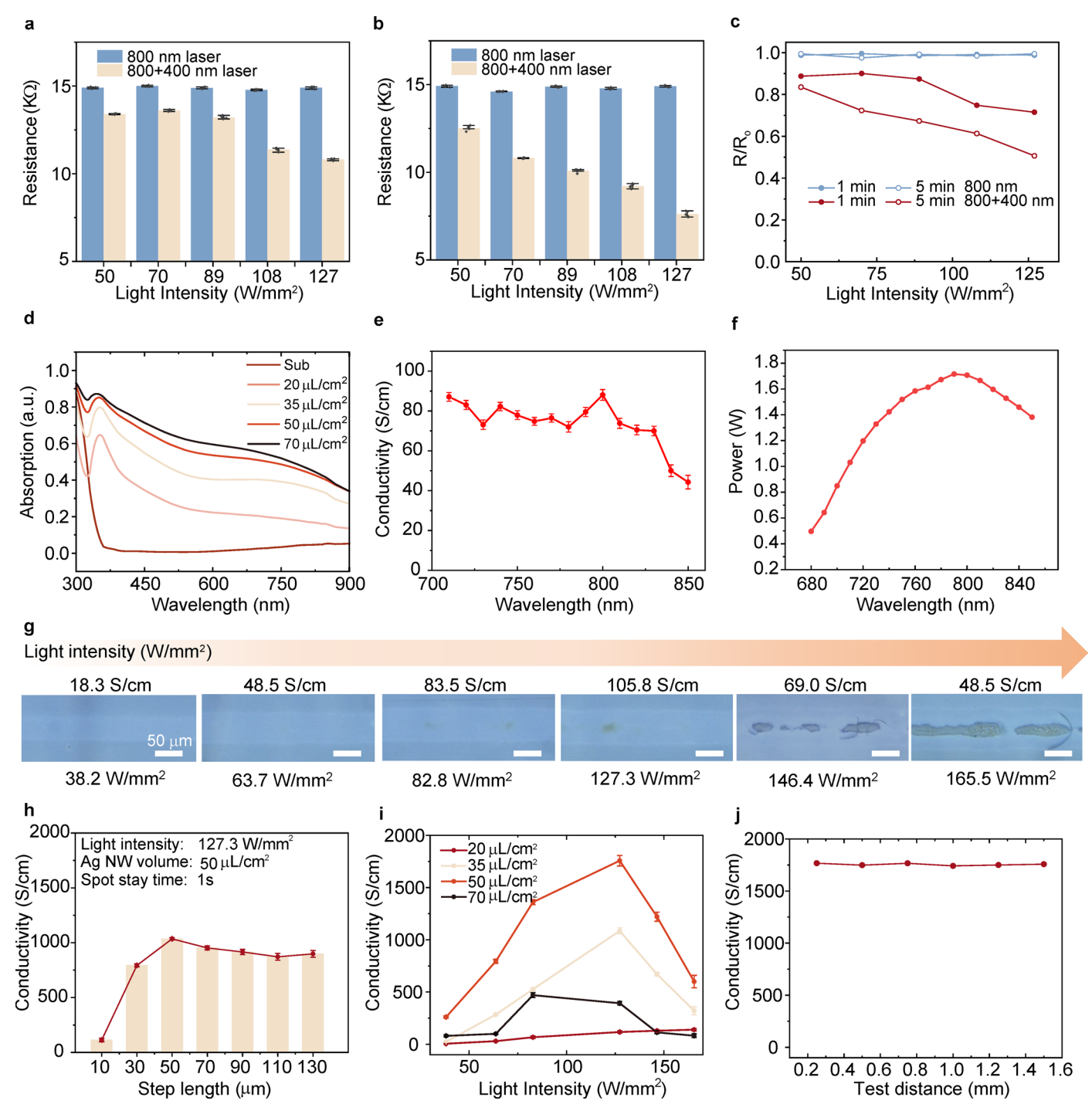
 $\textbf{Extended Data Fig. 3} \\ \textbf{| Electric field simulation for Ag NWs with side dumbbells. a}, \\ \textbf{Structure, coordinate, and incident light built in the simulation. b}, \\ \textbf{Electric field distribution profiles in the } \textbf{x-y plane for structures with varied length and side-dumbbell radius.} \\ \textbf{All of the } \textbf{x-y plane for structures with varied length and side-dumbbell radius.} \\ \textbf{All of the } \textbf{x-y plane for structures with varied length and side-dumbbell radius.} \\ \textbf{All of the } \textbf{x-y plane for structures with varied length and side-dumbbell radius.} \\ \textbf{All of the } \textbf{x-y plane for structures with varied length and side-dumbbell radius.} \\ \textbf{All of the } \textbf{x-y plane for structures with varied length and side-dumbbell radius.} \\ \textbf{All of the } \textbf{x-y plane for structures with varied length and side-dumbbell radius.} \\ \textbf{All of the } \textbf{x-y plane for structures with varied length and side-dumbbell radius.} \\ \textbf{All of the } \textbf{x-y plane for structures with varied length and side-dumbbell radius.} \\ \textbf{All of the } \textbf{x-y plane for structures with varied length and side-dumbbell radius.} \\ \textbf{All of the } \textbf{x-y plane for structures with varied length and side-dumbbell radius.} \\ \textbf{All of the } \textbf{x-y plane for structures with varied length and side-dumbbell radius.} \\ \textbf{All of the } \textbf{x-y plane for structures with varied length and side-dumbbell radius.} \\ \textbf{All of the } \textbf{x-y plane for structures with varied length and side-dumbbell radius.} \\ \textbf{All of the } \textbf{x-y plane for structures with varied length and side-dumbbell radius.} \\ \textbf{All of the } \textbf{x-y plane for structures with varied length and side-dumbbell radius.} \\ \textbf{All of the } \textbf{x-y plane for structures with varied length and side-dumbbell radius.} \\ \textbf{All of the } \textbf{x-y plane for structures with varied length and side-dumbbell radius.} \\ \textbf{All of the } \textbf{x-y plane for structures with varied length and side-dumbbell radius.} \\ \textbf{All of the } \textbf{x-y plane for structures with varied length and side-dumbbell radius.} \\ \textbf{All of the } \textbf{x-y plane for structures$ 



 $\textbf{Extended Data Fig. 4} \ | \ \textbf{O(1 s) XPS results of plasmonically printed MOs.} \ O(1 s) \ XPS \ results \ of \ plasmonically \ printed \ \textbf{a}, \ lnO_x, \ \textbf{b}, \ lGZO, \ \textbf{c}, \ AlOx, \ \textbf{d}, \ lZO.$ 

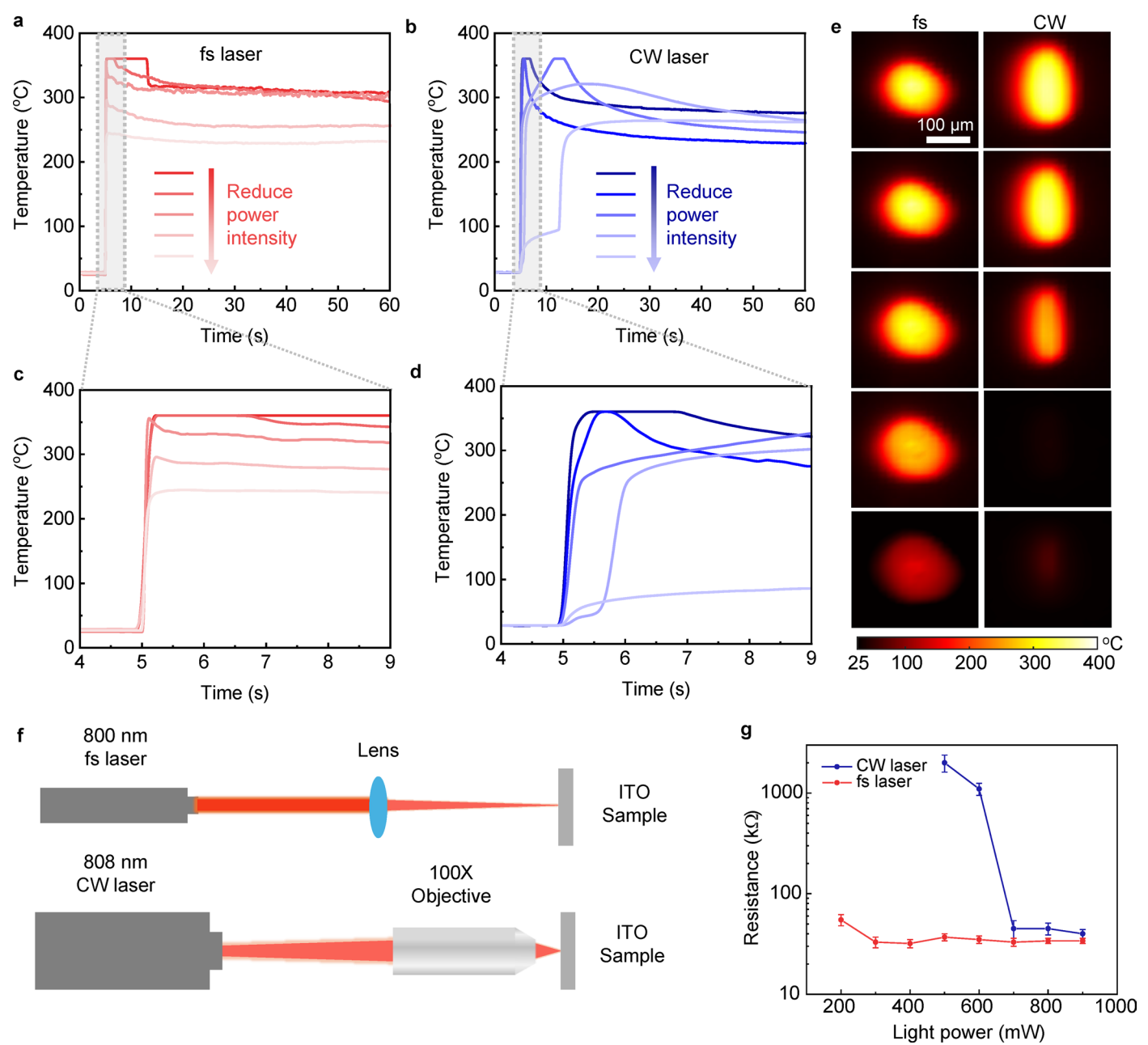


Extended Data Fig. 5 | GIAXRD results for 150 °C annealed, 400 °C annealed and plasmonically printed MOs. GIAXRD results for 150 °C annealed, 400 °C annealed and plasmonically printed a, ITO, b, AlO<sub>x</sub>, c, IGZO, d, InO<sub>x</sub> e, IZO.



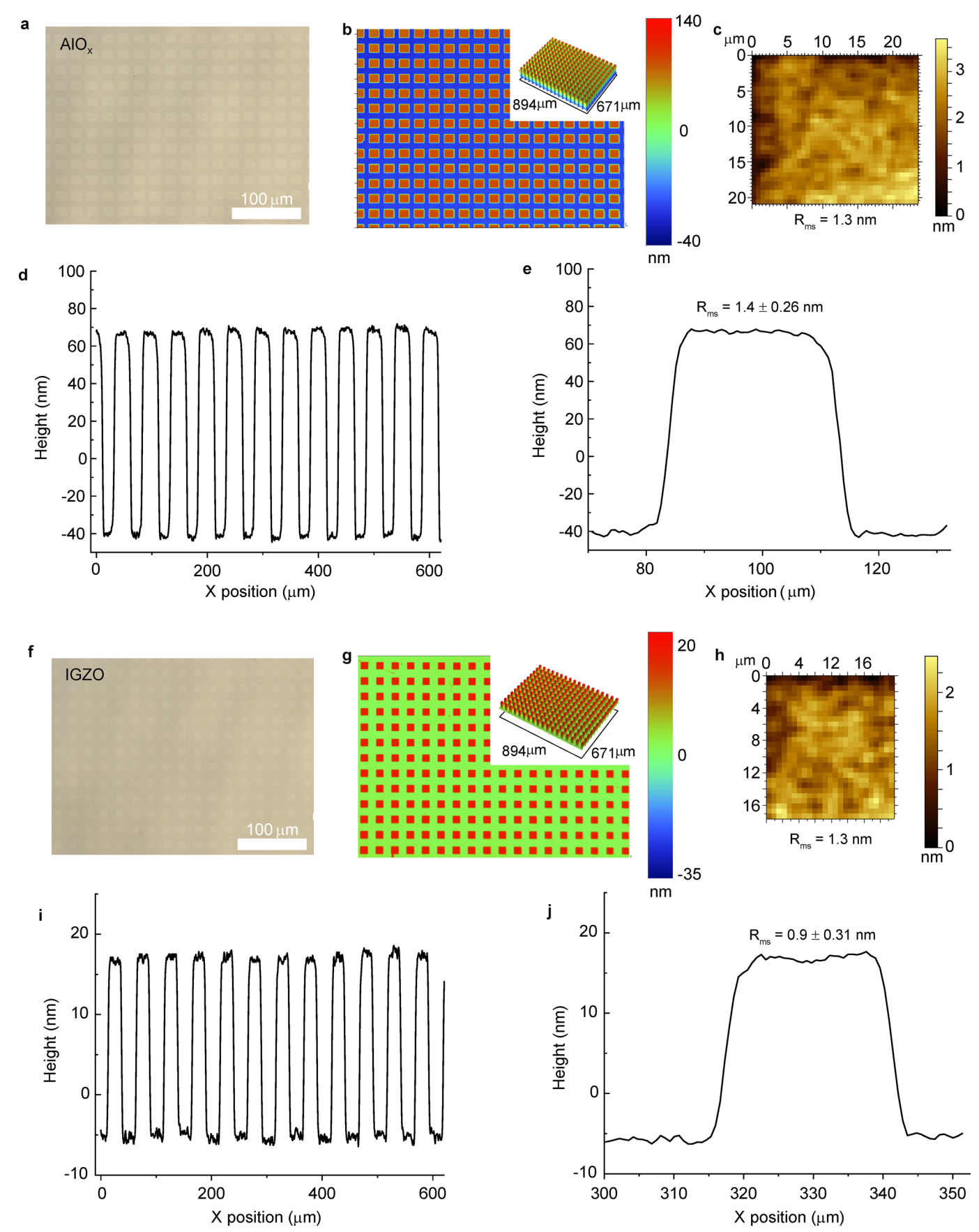
**Extended Data Fig. 6** | **Scanning parameter optimization of the plasmonic printing process.** Resistance (R) of an ITO film after laser irradiation (at 800 nm and 400 + 800 nm) under different light intensities for **a**, 1 min, **b**, 5 min. **c**, R/R<sub>o</sub> ratios extracted from **a** and **b**, with R<sub>o</sub> denoting the resistance of the ITO film before laser irradiation. Individual data points (n = 5 per group) are overlaid to show data distribution. Each point represents an independent ITO channel. Bar height, mean; error bars, standard deviation. **d**, Absorption spectra of Ag NW thin films at different thicknesses (controlled by the volume of Ag NW solution). **e**, Conductivity of a plasmonically printed ITO at varied fs laser wavelength. **f**, Output power of the fs laser at different wavelengths. **g**, Microscope

photographs and measured conductivity of plasmonically printed ITO channels using different light intensities. The beam-scanning step length in this experiment is  $10 \, \mu m$ . h, Conductivity of the plasmonically printed ITO channels using different beam-scanning step lengths. i, Conductivity of the plasmonically printed ITO channels of different thicknesses (controlled by the volume of Ag NW solution) using different light intensities. Data in e, h, i, are measured from 5 independent ITO channels per group. Bar height, mean; point, mean; error bars, standard deviation. (n = 5).j, Conductivity of the plasmonically printed ITO channels measured at varied test distance.



Extended Data Fig. 7 | Comparison on heating process and printed ITO performance between fs and CW lasers. a, b, Temporal temperature evolution during the plasmonic printing process respectively by fs laser and CW laser with varied power intensity, with the data collected right before and after laser illumination shown in c, d. e, Temperature distribution of the printed area after 0.1 s illumination by fs laser (left) and CW laser (right) with varied power intensity.

**f**, Schematics of the plasmonic printing optical setup using fs and CW lasers. The two laser beams are focused to the same size at the sample surface for direct comparison. **g**, Resistance of printed solution-processed ITO films under fs and CW lasers with varied light intensity. Data are measured from 5 independent ITO channels per group. Point, mean; error bars, standard deviation.



Extended Data Fig. 8 | Surface morphology of plasmonically printed high-density device arrays. a, Microscope photographs of a plasmonically printed high-density  ${\rm AlO}_{\rm x}$  array, with its optical surface profile shown in  ${\bf b}$  and extracted

height profile in  $\bf d$ .  $\bf c$  and  $\bf e$  show the optical surface profile and height profile of a single unit in the array.  $\bf f$ - $\bf j$ , Similar results as  $\bf a$ - $\bf e$  for a plasmonically printed high-density IGZO array.